

1 **Statistical Modeling and Characterization of Induced Seismicity within the Western**  
2 **Canada Sedimentary Basin**

3 **Sidhanth Kothari<sup>1</sup>, Robert Shcherbakov<sup>1</sup>, and Gail Atkinson<sup>1</sup>**

4 <sup>1</sup>Western University, London, Ontario, Canada

5  
6 Corresponding author: Sidhanth Kothari ([skothar3@uwo.ca](mailto:skothar3@uwo.ca))

7  
8 **Key Points:**

- 9 • Parts of western Canada have seen an increase in clustered seismic activity coinciding  
10 with the growing usage of hydraulic fracturing
- 11 • The regional seismicity can be subdivided into three main classes of inter-event distance  
12 using the nearest-neighbour distance method
- 13 • Analysis of earthquake clusters occurring near different types of anthropogenic  
14 operations reveal key differences in scaling and structure

15

**16 Abstract**

17 In western Canada, there has been an increase in seismic activity linked to anthropogenic energy-  
18 related operations including conventional hydrocarbon production, wastewater fluid injection  
19 and more recently hydraulic fracturing (HF). Statistical modeling and characterization of the  
20 space, time and magnitude distributions of the seismicity clusters is vital for a better  
21 understanding of induced earthquake processes and development of forecasting models. In this  
22 work, a statistical analysis of the seismicity in the Western Canada Sedimentary Basin was  
23 performed across past and present time periods by utilizing a compiled earthquake catalogue for  
24 Alberta and eastern British Columbia. Specifically, the inter-event space-time distance  
25 distributions of earthquakes were studied using the nearest-neighbour distance (NND) method.  
26 Additionally, the frequency-magnitude statistics and aftershock parameters of several clusters  
27 were analyzed using the Gutenberg-Richter relation and the epidemic type aftershock sequence  
28 model. The obtained results suggest that recent regional changes in the NND distributions,  
29 namely a disproportionate increase in loosely and tightly clustered seismic activity over time, are  
30 unnatural and likely due to the rise in HF operations for the development of unconventional  
31 resources. It is concluded that both these loosely and tightly clustered earthquake subpopulations  
32 differ measurably from what may be the region's tectonic seismic activity. Additionally, HF  
33 treatments have a greater probability of triggering swarm-like sequences that sharply spike the  
34 seismicity rate and are characterized by steeper frequency-magnitude distributions. Conventional  
35 production and wastewater disposal operations largely trigger loosely clustered activity with  
36 more typical magnitude-occurrence rates.

**37 Plain Language Summary**

38 In western Canada, there has been an increase in earthquake activity linked to industrial activities  
39 including fossil fuel extraction, wastewater disposal and more recently hydraulic fracturing.  
40 Statistical modeling of earthquake phenomena is important for the understanding of the specific  
41 mechanisms involved in triggering earthquakes. In this work, a statistical analysis of the  
42 recorded earthquakes in the Western Canada Sedimentary Basin is performed. The results of this  
43 study suggest that there are discrete statistical differences between the natural, tectonic  
44 earthquakes and those triggered artificially by human activity. Additionally, hydraulic fracturing  
45 operations appear capable of triggering swarm-like sequences that temporarily increase the

46 earthquake rate and tend to occur at small-to-moderate magnitudes. Conventional fuel production  
47 and wastewater disposal operations largely trigger earthquakes that are loosely clustered together  
48 in space and time across a broader magnitude range.

## 49 **1 Introduction**

### 50 1.1 Induced Seismicity

51 Human activities, such as hydrocarbon production, reservoir impoundment, mining and  
52 geothermal energy extraction, can alter subsurface stress regimes through a variety of  
53 mechanisms, including the withdrawal or injection of fluid, reservoir compaction, excess surface  
54 loading, and ground subsidence (Grigoli et al., 2017; Doglioni, 2018; Keranen & Weingarten,  
55 2018). In some cases, these stress perturbations result in earthquakes, particularly in areas  
56 characterized by higher states of stress and/or preexisting, well-oriented faults. This phenomenon  
57 is referred to as induced seismicity and is contributing to an increase in seismic hazard in certain  
58 parts of the world (Segall et al., 1995; Lei et al., 2008; Atkinson, 2017; McClure et al., 2017;  
59 Eaton et al., 2018; Brudzinski & Kozłowska, 2019).

60 In the central United States, for example, numerous earthquakes have been attributed to  
61 wastewater disposal wells operating in close proximity (Ellsworth, 2013; Llenos & Michael,  
62 2013; van der Elst et al., 2013; Keranen et al., 2014; Hornbach et al., 2016; Schoenball &  
63 Ellsworth, 2017). These wells inject large quantities of excess flow-back fluid from associated  
64 oil and gas production operations deep into underground reservoirs. This creates a pore pressure  
65 front that travels outward and may interact with fault structures, particularly in the crystalline  
66 basement where most of the associated seismic events occur (Horton, 2012; Ellsworth, 2013;  
67 Keranen et al., 2014; McClure et al., 2017; Shah & Keller, 2017). In the year 2016 alone,  
68 Oklahoma observed three earthquakes of moment magnitude ( $M$ )  $>5$ , including an  $M5.8$  event in  
69 Pawnee that was the largest event recorded in the state's history. All three events occurred within  
70 10 km of wastewater disposal wells and had moment releases that scaled with the net volume of  
71 near-field injection (McGarr & Barbour, 2017).

72 In parts of western Canada, there has been a notable rise in the seismic rate coinciding  
73 with the implementation of unconventional extraction technology developed for the production  
74 of oil and gas, known as hydraulic fracturing (HF) or “fracking” (B.C. Oil and Gas Commission,

75 2012, 2014; Schultz, Stern, Novakovic, et al., 2015; Atkinson et al., 2016; Bao & Eaton, 2016;  
76 Deng et al., 2016; Ghofrani & Atkinson, 2016; Schultz et al., 2016, 2017, 2018; Wang et al.,  
77 2016; Eaton et al., 2018; Zhang et al., 2019). During the HF process, fractures are created or  
78 enhanced within a target formation holding desired hydrocarbons, typically tight (low  
79 permeability) sedimentary layers, by the pumping of chemical slurry into segments of the rock  
80 over several stages. It is increasingly common for wells to be drilled at a deviated or horizontal  
81 angle as they approach a reservoir, in order to engage a larger portion of the source rock than  
82 would have been reached vertically. These technological advancements have prompted a  
83 dramatic growth in the number of possible fracture stages per wellbore as well as increased the  
84 average total volume of high-pressure fluid injected (King, 2010) and its areal extent. Between  
85 2010 and 2018, approximately 20,000 HF wells had been drilled horizontally within the Western  
86 Canada Sedimentary Basin (WCSB) (Atkinson et al., 2020). The associated rise in induced  
87 seismicity in western Canada appears highly clustered near some of these HF operations and  
88 cannot be fully accounted for by the deployment of denser seismic monitoring networks and  
89 more sensitive instruments (Schultz, Stern, Gu, et al., 2015; Atkinson et al., 2016; Cui &  
90 Atkinson, 2016). Furthermore, recent studies have demonstrated that the hazard related to  
91 induced seismicity, including HF, is potentially much greater than that of natural seismicity,  
92 particularly in areas characterized by low to moderate tectonic activity (Atkinson, 2017; Lee et  
93 al., 2019; Atkinson et al., 2020; Langenbruch et al., 2020).

## 94 1.2 Earthquake Clustering

95 Cases of induced seismicity commonly appear as earthquake clusters and can manifest as  
96 both mainshock-aftershock burst sequences and as seismic swarms. For example, the large  
97 wastewater disposal-induced events in Oklahoma triggered typical aftershock behavior,  
98 temporarily increasing the seismic rate due to the transfer of stress and brittle failure of the crust  
99 (Keranen et al., 2014; McGarr & Barbour, 2017). On the other hand, the HF-induced clustering  
100 near Youngstown, Ohio, and injection-related events in central Arkansas near Guy and  
101 Greenbrier displayed swarm-like characteristics, where the events were of similar magnitude and  
102 could not be attributed to any dominant mainshock (Horton, 2012; Llenos & Michael, 2013;  
103 Skoumal et al., 2015). Studies have shown that both natural and anthropogenic changes to the  
104 subsurface fluid content can enhance or induce earthquake sequences via subsidence and/or

105 changes in Coulomb fault stress and pore pressure conditions, especially near critically oriented  
106 structures (Segall, 1985; Langenbruch & Shapiro, 2010; Brodsky & Lajoie, 2013; Kumazawa &  
107 Ogata, 2013; Keranen et al., 2014; Goebel et al., 2015; Schoenball et al., 2015; Bao & Eaton,  
108 2016; Kettlety et al., 2019, 2020). The nature of clustering observed within a region may be  
109 attributed to its rheological structure, in the framework of viscoelastic deformation (Ben-Zion &  
110 Lyakhovskiy, 2006). In this context, a medium with low levels of heat flow and/or less fluid  
111 content correlate with higher viscosity and the conditions of brittle rheology, resulting in “burst-  
112 like” cracking of the crust and subsequent aftershock clustering. The converse is attributed to  
113 lower viscosity lithospheres of more brittle-ductile rheology (higher levels of heat and/or more  
114 fluid content), where failure is more likely to result in swarms of inter-linked events related to  
115 factors such as local fluid balance, destabilizing aseismic slip, and inter-event triggering  
116 (Zaliapin & Ben-Zion, 2016; Scuderi et al., 2017; Martínez-Garzón et al., 2018).

117 Identification of earthquake clustering involves a separation of the independent  
118 background rate from dependent event sequences (Gardner & Knopoff, 1974; Reasenber, 1985;  
119 Baiesi & Paczuski, 2004; Console et al., 2010; Ader & Avouac, 2013; Zaliapin & Ben-Zion,  
120 2013a; Schaefer et al., 2017). Due to the innumerable factors involved in the tectonic process,  
121 background seismicity may be approximated as random and modeled as a time-stationary, space-  
122 inhomogeneous marked Poisson process. Within this framework, rates of seismicity are assumed  
123 to vary in space but not in time and data points (seismic events) are marked by their magnitudes.  
124 Clustering, on the other hand, cannot be represented by a Poisson model, as the earthquake rate  
125 does not remain constant and depends in part on prior events. The separation of background and  
126 clustered earthquake phenomena is an important and non-trivial task required not only in cluster  
127 analysis but also in seismic hazard assessment, where catalogues are typically de-clustered in  
128 order to delineate source zones and assess recurrence parameters. The practical distinction of  
129 clustered and background seismicity should not restrict the consideration for potential interplay  
130 between them, particularly when external factors, such as anthropogenic activity, are involved.  
131 Induced seismicity has been observed to increase both the background rate and clustering  
132 productivity within affected regions (Lombardi et al., 2010; Llenos & Michael, 2013; Schoenball  
133 et al., 2015; Maghsoudi et al., 2016, 2018; Zaliapin & Ben-Zion, 2016; Vasylykivska & Huerta,  
134 2017; Martínez-Garzón et al., 2018). It is plausible that a rise in the former subsequently affects  
135 a rise in the latter.

136 For example, Llenos & Michael (2013) characterized both natural and fluid injection-  
137 induced swarms in Arkansas, namely the natural 1980s Enola sequence and the wastewater  
138 disposal-related 2010-2011 Greenbrier sequences, by applying the epidemic type aftershock  
139 sequence (ETAS) model (Ogata, 1988, 1989; Zhuang et al., 2004). The ETAS model estimates  
140 the time dependent seismic rate using the summation of a constant background term with a  
141 parameterized Omori-type aftershock kernel. Llenos & Michael (2013) found that the Enola and  
142 Greenbrier swarms could not be modeled using the same set of parameter values, with the  
143 induced cluster resulting in both a higher background rate and elevated aftershock productivity  
144 relative to the natural swarm. The authors proposed that variation in the absolute values of ETAS  
145 parameters may be a way to distinguish between natural and human-induced seismicity within  
146 the same region, particularly changes in the background rate parameter and magnitude-weighting  
147 factor. A comparable investigation was performed over the geothermal sites of Salton Sea and  
148 Brawley in southern California, and obtained similar results (Llenos & Michael, 2016).

149 Zaliapin & Ben-Zion (2013a, 2013b) analyzed multiple southern California earthquake  
150 catalogues, which contain a large amount of both natural (tectonic and magmatic) and man-made  
151 (geothermal energy production-related) seismicity, using the nearest-neighbour distance (NND)  
152 method (described in detail in section 3). Briefly, the NND approach links events to their closest  
153 ancestor, i.e. their “nearest neighbour”, based on a space, time, and magnitude-dependent metric.  
154 Events are separated into clusters (those that are strongly linked to their nearest neighbour) and  
155 background seismicity (those that are only weakly linked), whereby variation in relative mixing  
156 proportions between the two populations may be evaluated. Clusters may then be classified  
157 further into mainshock-aftershock “burst-like” sequences or inter-event triggered “swarm-like”  
158 sequences, using their distinguishable structural characteristics. Zaliapin & Ben-Zion (2013a,  
159 2013b), along with Hicks (2011), found that a natural separation occurs between clustered and  
160 background events for many regional catalogues, as well as for worldwide seismicity.  
161 Furthermore, the authors found that events within the clustered mode largely exhibit  
162 characteristics of either burst or swarm-like sequences. Their studies agreed well with the  
163 viscoelastic damage model, where a higher degree of inter-event triggering and swarm-like  
164 clustering was found within more ductile regions, such as geothermal settings or areas prone to  
165 magmatic or dike intrusion (e.g. Sagiya et al., 2002; Morita et al., 2006; Farrell et al., 2009),  
166 whereas more brittle rheology tended toward a higher proportion of burst-like sequences.

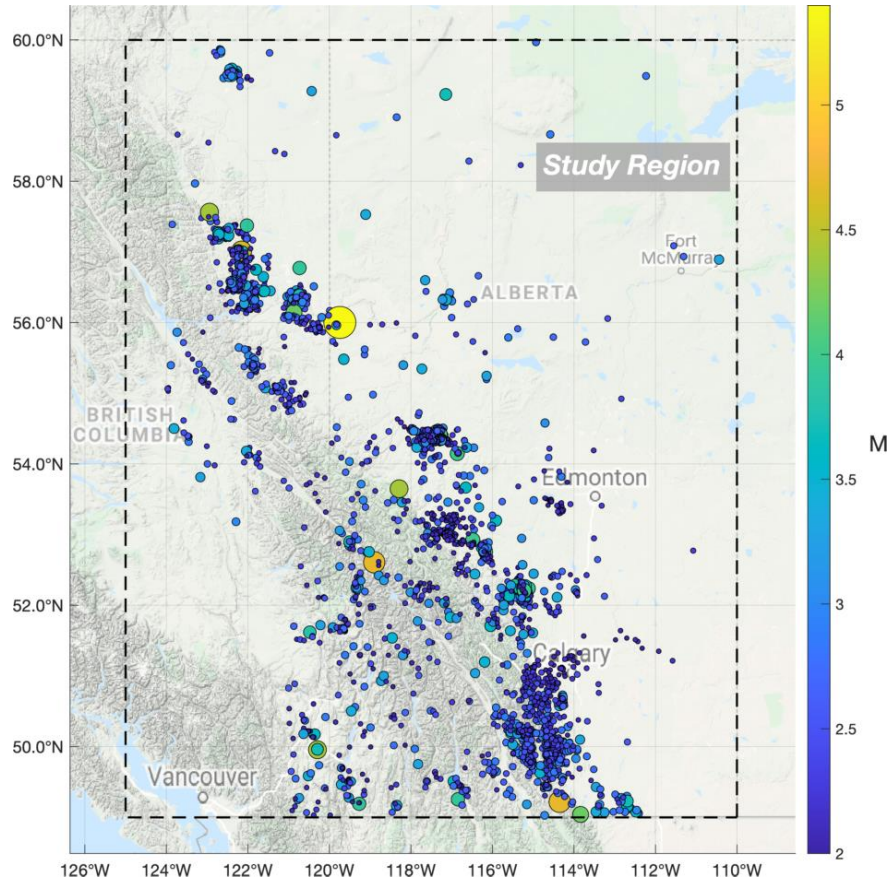
## 167           1.3 Study Area and Motivation

168           This study focuses on Alberta and eastern British Columbia, where seismicity has been  
169 low historically, with the majority of tectonic events occurring along the foreland belt of the  
170 Rocky Mountain range (Rogers & Horner, 1991). However, isolated incidents of induced  
171 spatiotemporally clustered seismicity have been documented. Baranova et al. (1999) and Eaton  
172 & Mahani (2015) linked the earthquake clustering near Rocky Mountain House, Alberta, to a  
173 depletion of pore pressure and an accumulation of compaction-related stress beneath the nearby  
174 Strachan gas extraction field between the 1970s and 1990s. In the 1980s and 1990s, fluid  
175 injection for secondary oil recovery and wastewater disposal had most likely triggered  
176 earthquake clustering northwest of Fort St. John, B.C. (Horner et al., 1994). More recently, HF  
177 and wastewater injection has taken place within the Montney and Horn River Basin shale  
178 formations; these operations are suspected to be contributing to the growth of seismic activity in  
179 that area based on spatiotemporal links to well activity as well as identification of nearby  
180 subsurface fault channels (B.C. Oil and Gas Commission, 2012, 2014). Further, several studies  
181 have provided evidence relating the extended HF-related fluid injection within the Duvernay  
182 formation to the recent seismicity west of Fox Creek, Alberta, via pore pressure increase and  
183 poroelastic stress perturbation. These events began in December 2013 as a series of clusters near  
184 Crooked Lake and continue to transpire intermittently to the present day (Schultz, Stern,  
185 Novakovic, et al., 2015; Bao & Eaton, 2016; Wang et al., 2016; Schultz et al., 2017; Zhang et al.,  
186 2019).

187           While many other studied regions tend to have a single dominant mechanism driving  
188 most of the induced earthquake activity, such as large-scale wastewater disposal in the central  
189 United States (Horton, 2012; Ellsworth, 2013; Llenos & Michael, 2013; van der Elst et al., 2013)  
190 or the geothermal energy operations in southern California (Brodsky & Lajoie, 2013; Zaliapin &  
191 Ben-Zion, 2013a), the WCSB is characterized by a multiplicity of local triggering mechanisms.  
192 The low natural occurrence rate has allowed for a relatively straightforward identification of the  
193 recent surge in unnatural seismicity (e.g. Atkinson et al., 2016), in comparison to the situation in  
194 other regions (e.g. Schoenball et al., 2015). Moreover, the increased seismicity may be  
195 particularly consequential in low-hazard regions where facilities were not designed for high  
196 seismic levels (Atkinson et al., 2020). These factors offer significant motivation to analyze the  
197 regional changes in earthquake space, time, and magnitude distributions statistically. It is also

198 worthwhile to compare the different clusters and their potential triggers, particularly past cases of  
199 conventional production and disposal-related earthquakes versus the recent seismicity triggered  
200 by hydraulic fracturing. In this paper, we aim to characterize the regional and clustered  
201 earthquakes using data from the Composite Alberta Seismicity Catalogue (CASC, described in  
202 section 2) via the application of the nearest-neighbour distance method. The objectives are  
203 twofold. The first is to demonstrate fundamental differences in the regional seismicity  
204 distributions over time and the second is to illuminate specific features of induced seismicity  
205 clustering that could be expected or recognized when performing certain types of operations,  
206 particularly hydraulic fracturing.

207         In the following sections, background information is provided on the regional earthquake  
208 catalogue and on four particular areas of earthquake clustering suspected to have been triggered  
209 by nearby human operations (section 2). The nearest-neighbour distance methodology is  
210 described (section 3). Analysis of the regional catalogue over time is presented (section 4);  
211 scaling relationships and statistical properties of the four clustering sites are discussed (section  
212 5). A discussion and comparison with other, similar regional studies (section 6) is followed by a  
213 brief summary (section 7).

214 **2 Data and Study Regions**215 **2.1 Earthquake Catalogue**

216

217 *Figure 1: Map of  $M_{2+}$  seismic events documented by the Composite Alberta Seismicity Catalogue (CASC) from 1975-2018.*  
 218 *Marker size and colour indicate earthquake moment magnitude.*

219 The Composite Alberta Seismicity Catalogue (CASC), available online at  
 220 [www.inducedseismicity.ca](http://www.inducedseismicity.ca), contains seismic event records from the early 1900s through to the  
 221 present. The spatial boundaries of the region encompass a rectangular area spanning [49° –  
 222 60°N] and [110° – 125°W], including the entirety of Alberta and a portion of eastern British  
 223 Columbia (Figure 1). The CASC is compiled from several contributing agencies operating across  
 224 Alberta and eastern British Columbia, including the Geological Survey of Canada and  
 225 Earthquakes Canada ([www.seismo.nrcan.gc.ca](http://www.seismo.nrcan.gc.ca)), the Alberta Geological Survey and the Regional  
 226 Alberta Observatory for Earthquake Studies ([ags.aer.ca](http://ags.aer.ca)), the Canadian Rockies and Alberta  
 227 Network ([ds.iris.edu](http://ds.iris.edu)), and the TransAlta/Nanometrics Network ([www.nanometrics.ca](http://www.nanometrics.ca)). The  
 228 catalogue contains information concerning the date, time, estimated geographic location,

229 magnitude, magnitude scale, and moment magnitude conversion for each detected event  
230 occurrence (for a detailed discussion on the compilation of the CASC, see Cui et al. (2015)). The  
231 database is estimated to be complete to the moment magnitude  $M \approx 3$  level from 1985 onward  
232 (Adams & Halchuk, 2003; Cui & Atkinson, 2016). Seismic network coverage is generally  
233 spatiotemporally inhomogeneous and so local completeness levels over a given time period may  
234 be substantially lower than the regional completeness; this matter is explored in the cluster  
235 analyses in section 5. Accurate depth estimations remain a difficult task for most networks and,  
236 as a consequence, depths listed in this catalogue have large errors or are only specified as default  
237 values. While hypocentral locations would be beneficial for statistical analyses in three  
238 dimensions, they are not critical. The methods used in this study require relatively few input  
239 requirements; only the magnitudes, epicentral locations and times of occurrence are used from  
240 the database.

241         Some potential artifacts related to catalogue inconsistencies are important to note. First,  
242 many of the seismic recordings within the CASC are nontectonic and instead a product of quarry  
243 and mining blasts. These events are generally flagged by network personnel based on several  
244 criteria, including event time (blasts occur during daylight hours), proximity to active mines and  
245 quarries, and specific waveform characteristics (typically compressional first motions and high  
246 frequency spectra) (Cui et al., 2015; Schultz, Stern, Gu, et al., 2015; Cui & Atkinson, 2016). In  
247 this study, all flagged events were removed from the catalogue beforehand. However, recent  
248 blast events (after 2014), southwest of Calgary, had not yet been flagged by the network at the  
249 time of access (last accessed June 2020, [www.inducedseismicity.ca](http://www.inducedseismicity.ca)) and were hence included in  
250 the analyses. A second potential artifact is that the CASC is spatially limited to the Alberta  
251 region and only a portion of northeastern B.C. This explains the lack of recorded events  
252 surrounding the Vancouver area in Figure 1. Readers interested in documented seismicity west of  
253 Alberta are referred to the National Earthquakes Database ([database link](#)).

## 254         2.2 Induced Earthquake Clusters

### 255         The Rocky Mountain House cluster (RMHC)

256         One of the first significant instances of induced seismicity within the WCSB occurred  
257 approximately 25 km southwest of the town of Rocky Mountain House, Alberta. The area had

258 been historically quiescent before the onset of conventional gas production within the Duvernay  
259 formation in the early 1970s (Rogers & Horner, 1991). It became active predominantly from  
260 1975-1992, lagging production rates by several years and returning to apparent background  
261 activity by the year 2000. Wetmiller (1986) found that the majority of events occurred roughly  
262 within a 15 km radius and were concentrated close to the Strachan and Ricinus gas fields.  
263 Baranova et al. (1999) proposed that the earthquakes were triggered due to long-term  
264 compaction-related changes in the stress field caused by the extraction of fluid. We refer to this  
265 collection of events between 1975-2000 as the RMHC (Figure S1).

#### 266 The Montney clusters (MC1 & MC2)

267         Conventional oil and gas production has occurred within the Montney formation, which  
268 stretches across northeastern British Columbia and northwestern Alberta, since the 1950s.  
269 Associated wastewater disposal wells have been active from the 1960s and are suspected to have  
270 triggered two distinct earthquake clusters (Horner et al., 1994; B.C. Oil and Gas Commission,  
271 2014). The first began in 1984, north of the town Fort St. John, B.C., and the second began in  
272 2003, west of Halfway Ranch, B.C. We collectively refer to these two clusters, occurring  
273 predominantly between 1984-2009, as the MC1.

274         Since the mid-to-late 2000s, with the development of horizontal drilling and HF  
275 technology, the Montney trend has attracted significant interest for its siltstone and shale gas  
276 reserves. By 2018, thousands of natural gas wells were active in the area, operating along the  
277 formation's northwestern margin as well as to the southeast near Dawson Creek, B.C. In  
278 addition, more than 15 wastewater disposal wells have been drilled since 2005, bringing the  
279 formation's total to over 100 (B.C. Oil and Gas Commission, 2014). Since then, substantial low-  
280 to-moderate seismicity has been recorded in the area, due to the augmentation of the local  
281 seismic network and possibly the increase in subsurface human activity. The distribution of  
282 events occurring in the formation has changed over time, as the dominant triggering mechanism  
283 shifted from wastewater injection to HF (B.C. Oil and Gas Commission, 2014; Atkinson et al.,  
284 2016). We refer to the recently recorded seismicity in this area, from 2010 to 2018, as the MC2.

## 285 The Fox Creek Cluster (FCC)

286 Conventional production in central Alberta, primarily within the Duvernay, Swan Hills  
287 and Leduc formations, has been occurring since the 1960s and resulted in minor associated  
288 seismicity apart from the clustering near Rocky Mountain House. However, in December 2013,  
289 earthquakes began occurring approximately 30-40 km west of the town of Fox Creek, Alberta,  
290 where HF wells had recently been drilled in order to access the Duvernay's reservoirs of tight  
291 shale. Several hundreds of these wells have been drilled since 2012, near the recent clustering,  
292 and a large proportion were drilled horizontally or at a deviated angle. Seismic activity began as  
293 a few distinct sequences near Crooked Lake, Alberta, and continues to form further clusters up to  
294 the present day (Bao & Eaton, 2016; Clerc et al., 2016; Deng et al., 2016; Schultz et al., 2016,  
295 2017, 2018; Wang et al., 2016; Eaton et al., 2018; Zhang et al., 2019). We refer to this group of  
296 events, from 2013 to January 2020, as the FCC.

297 We focus our study on these four clusters, as their seismicity is sufficiently rich for  
298 analysis. New clusters continue to emerge, such as those in the area near Red Deer, Alberta (e.g.  
299 Schultz et al., 2020).

## 300 **3 The Nearest-Neighbour Distance Method**

301 The nearest-neighbour distance (NND) method is a statistical approach to earthquake  
302 cluster identification and classification, first formulated by Baiesi & Paczuski (2004) and  
303 expanded significantly by Zaliapin et al. (2008) and Zaliapin & Ben-Zion (2013a, 2013b, 2016).  
304 Its purpose is to link together and characterize *event families* or *sequences* using a rescaled inter-  
305 event distance metric termed the nearest-neighbour distance  $\eta$ , which is defined below as space,  
306 time and magnitude dependent. This method is applied in sections 4 and 5 in order to describe  
307 the regional and local inter-event distance distributions within the WCSB as well as to  
308 statistically categorize the types of seismic clustering observed.

### 309 3.1 The Rescaled Inter-Event Distance Metric $\eta$

310 The inter-event distance values  $\eta_{ij}$  are defined based on the spatiotemporal distance  
311 between each event pair within the catalogue as well as on the magnitude of the event that  
312 occurred *first* (the potential *parent* event  $i$ ). Specifically, each event  $j$  is assigned values  $\eta_{ij}$  based  
313 on its relationship with all other events  $i$  as

$$\eta_{ij} = \begin{cases} t_{ij}(r_{ij})^{d_f} 10^{-bm_i}, & t_{ij} > 0 \\ \infty, & t_{ij} \leq 0 \end{cases}, \quad [1]$$

314 where  $t_{ij} = t_j - t_i$  is the time in days between event  $j$  and event  $i$ . Note that event  $j$  must  
 315 succeed event  $i$  in order for the quantity  $t_{ij}$  to be positive, otherwise  $\eta_{ij} = \infty$ .

316 The inter-event spatial distance  $r_{ij}$  is computed between epicenters using the Haversine  
 317 formula for great-circle distance (or arc length) in kilometers

$$r_{ij} = 2r_e \arcsin \sqrt{\sin^2 \frac{(\varphi_i - \varphi_j)}{2} + \cos \varphi_i \cos \varphi_j \sin^2 \frac{(\lambda_i - \lambda_j)}{2}}. \quad [2]$$

318 In Equation [2],  $r_e$  is the Earth's radius estimated as 6378.14 km, and  $(\varphi_i, \lambda_i)$  and  $(\varphi_j, \lambda_j)$  are the  
 319 latitudinal and longitudinal coordinates of events  $i$  and  $j$ , respectively.

320  $d_f$  is the fractal spatial dimension of earthquake epicenter distribution. In 2 dimensions,  
 321 for both local and worldwide epicentral distributions,  $d_f$  has been found to vary approximately  
 322 between 1.2 and 1.6 (Sadovsky et al., 1984; Kagan, 1991; Kosobokov & Mazhkenov, 2013).  $m_i$   
 323 is the magnitude of the  $i^{\text{th}}$  event and  $b$  is the Gutenberg-Richter  $b$ -value, which approximates the  
 324 exponential distribution of magnitude scaling according to

325

$$N(\geq M) = 10^{a-b(M-M_0)}; M \geq M_0, \quad [3]$$

326 where  $N(\geq M)$  is the number of detected events greater than or equal to magnitude  $M$  and  $a$   
 327 reflects the rate of seismicity over the time period considered.

328

329

330

331

332 The scalar distance  $\eta_{ij}$  may be expressed in terms of its rescaled temporal and spatial  
 333 components by defining

$$T_{ij} = t_{ij} 10^{-\frac{bm_i}{2}};$$

$$R_{ij} = r_{ij}^{df} 10^{-\frac{bm_i}{2}}.$$
[4]

334 By this formulation,  $\eta_{ij} = T_{ij}R_{ij}$ . Once nearest-neighbour values  $\eta$  have been determined for  
 335 each event  $j$ , where  $\eta_j = \min_{i < j} \eta_{ij}$ , the  $\eta$  distribution, the joint distribution of  $(T, R)$  as well as  
 336 their individual histograms can be plotted to observe possible modality in the temporal and/or  
 337 spatial distance between events. Hicks (2011) showed that a bimodal distribution in  $\eta$ ,  
 338 interpreted as a distinction between background and clustered events, is an intrinsic property of  
 339 both worldwide and regional seismicity. The clustered mode is identified as the subpopulation of  
 340 events occurring at small  $\eta$  values (small inter-event distances); these events are considered to be  
 341 strongly linked to their nearest neighbours. The background mode is identified as the set of  
 342 events occurring at larger  $\eta$  values (larger inter-event distances); these events are considered to  
 343 be only weakly linked to their nearest neighbours.

### 344 3.2 Formal Analysis of Modality in the $\eta$ Distribution

345 Although the subpopulations of clustered and background events may be apparent upon  
 346 visual inspection, it is useful to define them rigorously considering a Gaussian mixture model  
 347 (GMM), as detailed in Hicks (2011). A GMM is defined as a composition of normal density  
 348 functions, each with a mean, covariance and mixing proportion (or weight). The parameters for  
 349 these component functions are estimated using the 2-step expectation-maximization algorithm  
 350 (Hastie et al., 2009). The approach uses an initial guess for the set of parameters to then:

- 351 a) Calculate Bayesian probabilities for each data point as a possible member of each  
 352 mode. This is the expectation step.
- 353 b) Estimate the model parameters for each mode through their maximum likelihood  
 354 function, using the probabilities determined in the expectation step as weights. This is  
 355 the maximization step.

356 This process is iterated until it converges to the optimal estimation of the means, standard  
 357 deviations and weights. The number of modes in the distribution is determined using information  
 358 criteria. The model that minimizes the information criteria is considered the best fit. Two such  
 359 criteria were used in this study, the Akaike and Bayesian information criteria (Akaike, 1974;  
 360 Schwarz, 1978). The threshold value  $\log_{10} \eta_{thresh}$ , which separates the background mode from  
 361 the clustered mode, is chosen as the intersection point between the resulting component  
 362 densities.

### 363 3.3 Event-Family Classification

364 By removing all weak links from the NND distribution, the clustered mode may be  
 365 further discretized into hierarchical families based on the strong links between parents and  
 366 offspring events. The largest event in each family is classified as the mainshock; if there is more  
 367 than one largest-magnitude event then the first is considered the mainshock. Events in the  
 368 sequence that occur before the mainshock are called foreshocks and occur after are called  
 369 aftershocks. An aftershock's *generation*, or *order*, is determined by its hierarchical distance from  
 370 the mainshock. For example, an aftershock whose parent event is the mainshock is considered 1<sup>st</sup>  
 371 generation, while an aftershock whose parent event is a 1<sup>st</sup> generation aftershock is considered  
 372 2<sup>nd</sup> generation, and so on.

373 These families can be categorized as aftershock sequences, seismic swarms, a  
 374 combination of the two, or neither, based on statistical parameters introduced by Zaliapin & Ben-  
 375 Zion (2013b). These parameters quantify the structural characteristics of each event family and  
 376 can determine their structure type. The terminology of a rooted tree-graph is employed, which  
 377 considers the first event in a sequence as the *root* of the tree, the downward-directed edges  
 378 connecting events as *branches* and the end-nodes (earthquakes that have no further offspring) as  
 379 *leaves*. The size  $N$  is computed as the number of events in a sequence. The *leaf depth*  $d$  is  
 380 calculated by counting the number of branches connecting each leaf back to its root. The *average*  
 381 *leaf depth*  $\langle d \rangle$  of a particular tree provides an indication of its shape, with larger  $\langle d \rangle$  potentially  
 382 indicating higher levels of event chaining and a deeper structure, and smaller  $\langle d \rangle$  implying low  
 383 orders of event offspring and a shallower structure. Therefore, swarm sequences are expected to  
 384 have larger  $\langle d \rangle$  values than bursts, even given a similar number of leaves. However, since  $\langle d \rangle$   
 385 scales with the sequence size  $N$ , a normalized leaf depth  $\delta$ , where  $\delta = \frac{\langle d \rangle}{\sqrt{N}}$ , is also calculated. The

386 *inverted branching number*  $B_I$  of a tree is computed as the number of parent events divided by  
387 the total number of branches. A maximum  $B_I$  value of unity indicates a perfect path shape and  
388 only a single leaf within the structure. Smaller values of  $B_I$  imply more offspring from fewer  
389 parents, i.e. a more burst-like formation. The *magnitude differential*  $\Delta m$  is defined as the  
390 difference between the designated mainshock and second-largest event in a sequence. Generally,  
391 aftershock sequences tend to have larger  $\Delta m$  values than swarms, given a similar size  $N$ . In  
392 addition, we compute the *spatial area*  $A$  (in  $km^2$ ) and *time period*  $t_D$  (in days) covered by each  
393 family. However, these parameters also scale with  $N$  and are included for observational purposes  
394 only.

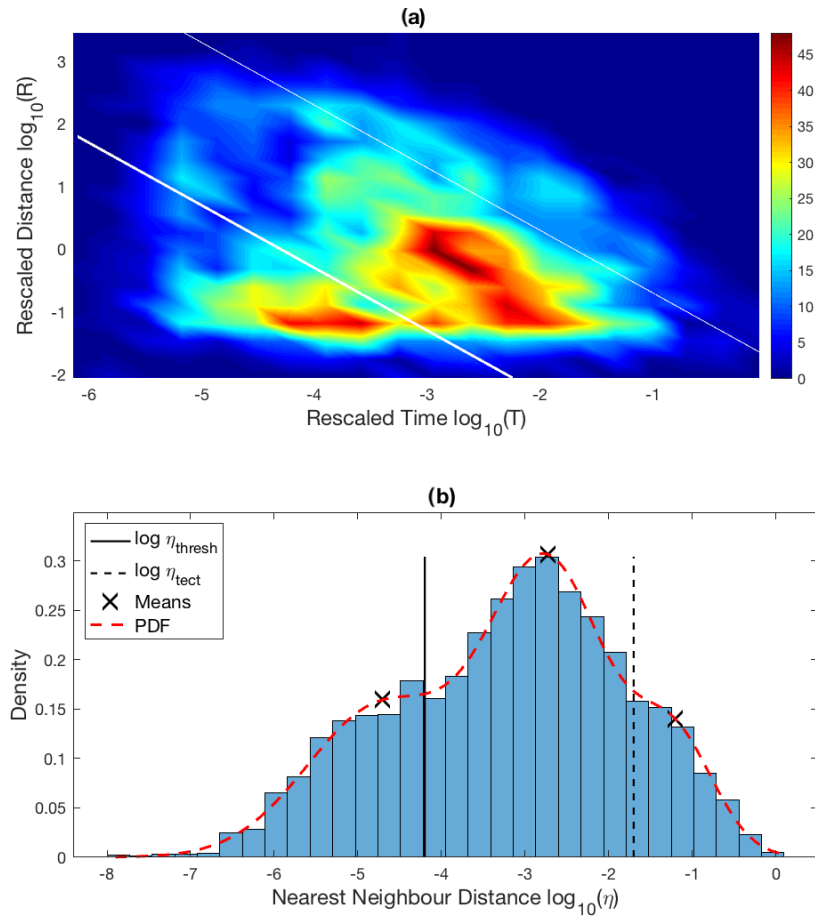
#### 395 **4 Regional Analysis of NND Distributions within the WCSB**

396 In this section, we applied the nearest-neighbour distance (NND) method to the regional  
397 Composite Alberta Seismicity Catalogue (CASC; detailed in section 2). The entire time period,  
398 between 1975-2018, was analyzed, as were separated time windows, between 1975-2009 and  
399 2010-2018. The separation between time frames was chosen to correspond with the rapid rise in  
400 hydraulic fracturing implementation that occurred within the region after 2009 (e.g. Atkinson et  
401 al., 2016, 2020)

402 Zaliapin & Ben-Zion (2013a, 2013b) showed that NND distributions are stable for cut-off  
403 magnitudes below the regional completeness magnitude ( $M_c \approx 3.0$  in this case); we therefore  
404 applied a magnitude cut-off of  $M_0 = 2.0$  to enrich sampling. Figures S5-8 show that the results  
405 found here hold for cut-off magnitudes up to the regional completeness level. The same constant  
406 values  $d_f = 1.5$  and  $b = 1.0$  were used for each subset of the regional data to illustrate the  
407 fundamental differences observed over time without prior parameterization.

408

## 4.1 Entire Time Period (1975-2018)



409

410 **Figure 2:** NND distribution of the regional WCSB catalogue (1975-2018) using  $M_0 = 2.0$ . a) Joint distribution of the temporal  
 411 and spatial components ( $T,R$ ). Bold white line indicates the threshold  $\log_{10} \eta_{\text{thresh}}$  between tightly clustered and loosely  
 412 clustered components. Thin white line indicates the threshold  $\log_{10} \eta_{\text{tect}}$  between loosely clustered and deep-background  
 413 components. Colour bar indicates frequency of inter-event distance occurrence. b) Normalized density of  $\eta$  values. Solid black  
 414 line is  $\log_{10} \eta_{\text{thresh}}$  and dashed black line is  $\log_{10} \eta_{\text{tect}}$ . Dashed red line is the normalized probability density function of the  
 415 Gaussian mixture and black crosses are the component means.

416 Figure 2 shows the 2-dimensional ( $T,R$ ) distribution and the normalized density of  
 417 nearest-neighbour distances  $\eta$  for the entire study period. There are two prevailing modes within  
 418 the joint distribution (Figure 2a), which differ in size and shape. The clustered mode, to the  
 419 bottom-left of the plot beneath the bold white line, is oriented somewhat horizontally, while the  
 420 background mode, in between the two white lines, covers a broader range along the  $T$  and  $R$  axes  
 421 and is faintly oriented along the downward diagonal. This observation is consistent with most  
 422 findings in other studies, which showed the existence and distinct shaping of clustered and

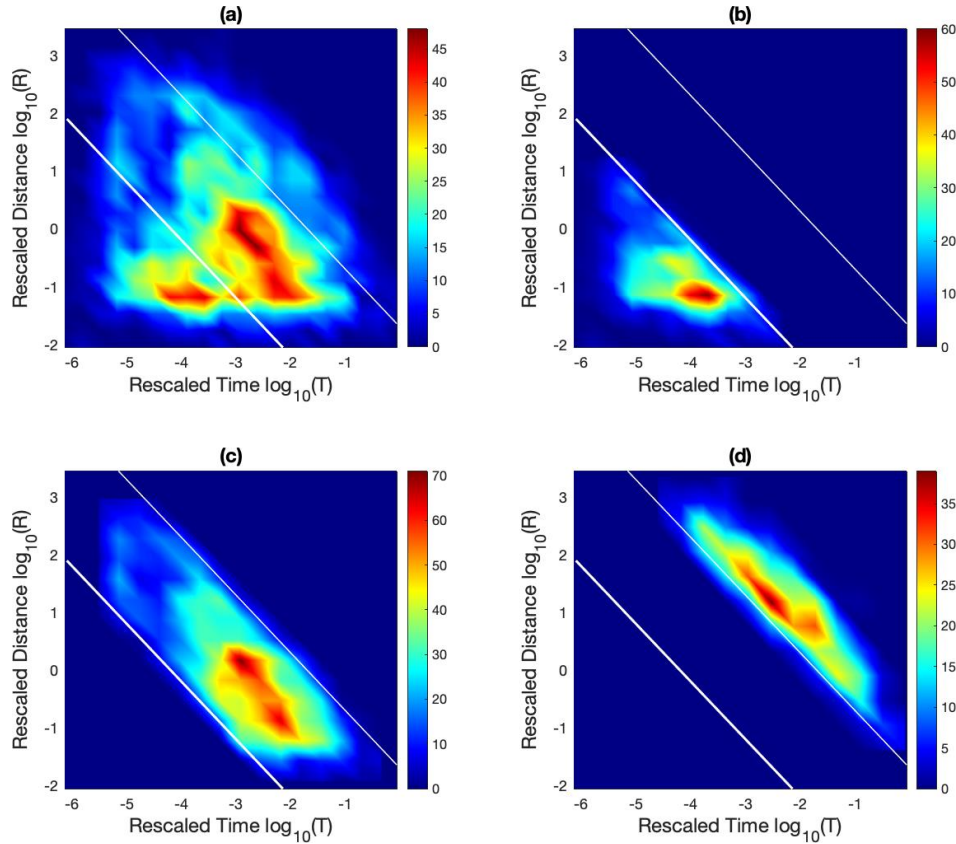
423 background earthquake subpopulations in several tectonic and induced areas (Hicks, 2011;  
 424 Zaliapin & Ben-Zion, 2013a, 2016; Schoenball et al., 2015). Notably, in these cases the  
 425 background mode was reminiscent of a time-stationary, space-inhomogeneous marked Poisson  
 426 process, which forms a unimodal distribution concentrated along a downward diagonal at large  $T$   
 427 and  $R$ , while the clustered mode typically occupies an ellipse at smaller  $T$  and  $R$  values than  
 428 would be expected from a Poisson process (Zaliapin & Ben-Zion, 2013a). The chief disparity  
 429 between different regions, including within the WCSB, lies in the relative intensities, or mixing  
 430 proportions, of each mode; these proportions tend to reflect the nature of seismicity occurring  
 431 (discussed further below). More difficult to see in Figure 2a is a third subpopulation, to the  
 432 upper-right above the thin white line, which is much less concentrated and sprawls along a  
 433 downward diagonal over large values of  $T$  and  $R$ . The one-dimensional  $\eta$  distribution (Figure 2b)  
 434 reflects this tri-modality clearly, with the third mode at large  $\eta$  perhaps more apparent.

435 The results of the Gaussian mixture model analyses indicate that the optimal mixture  
 436 estimation, i.e. a minimization of the information criteria, is a 3-component, instead of the  
 437 typically observed 2-component (clustered and background), distribution. This may be observed  
 438 in Figure 2b, where the dashed red line and black crosses represent the resulting probability  
 439 density function and 3 component means, respectively.

440 The intersection point between the two dominant modes occurs at  $\log_{10} \eta_{thresh} = -4.2$ ,  
 441 shown by the bolded white line in Figure 2a, and solid black line in Figure 2b. Out of the 3531  
 442 total events analyzed, 29% were found in the clustered domain, which is henceforth referred to  
 443 as the *tightly clustered* mode. 56% were located in the middle mode, which is henceforth referred  
 444 to as the *loosely clustered* mode, and 15% were located in the third mode at large  $\eta$ , henceforth  
 445 referred to as the *deep background*. The intersection between the loosely clustered and deep  
 446 background modes occurs at  $\log_{10} \eta_{tect} = -1.7$ , shown by the thin white line in Figure 2a, and  
 447 dashed black line in Figure 2b. No definitive trends were apparent in the individual  $T$  or  $R$   
 448 distributions (not shown), with the exception of an increasing proportion of small  $R$  distances  
 449 that tended to stack at the limits of network location resolution, giving the tightly clustered mode  
 450 its azimuthal shape. This agrees with another observation of Zaliapin & Ben-Zion (2013a), who  
 451 state that the modality in  $\eta$  cannot be fully explained by marginal trends present in either  $T$  or  $R$

452 but is in fact dependent on the association between the two, as seen in the 2-dimensional joint  
 453 distribution.

#### 454 4.1.1 Comparative Analysis of Mixture Components

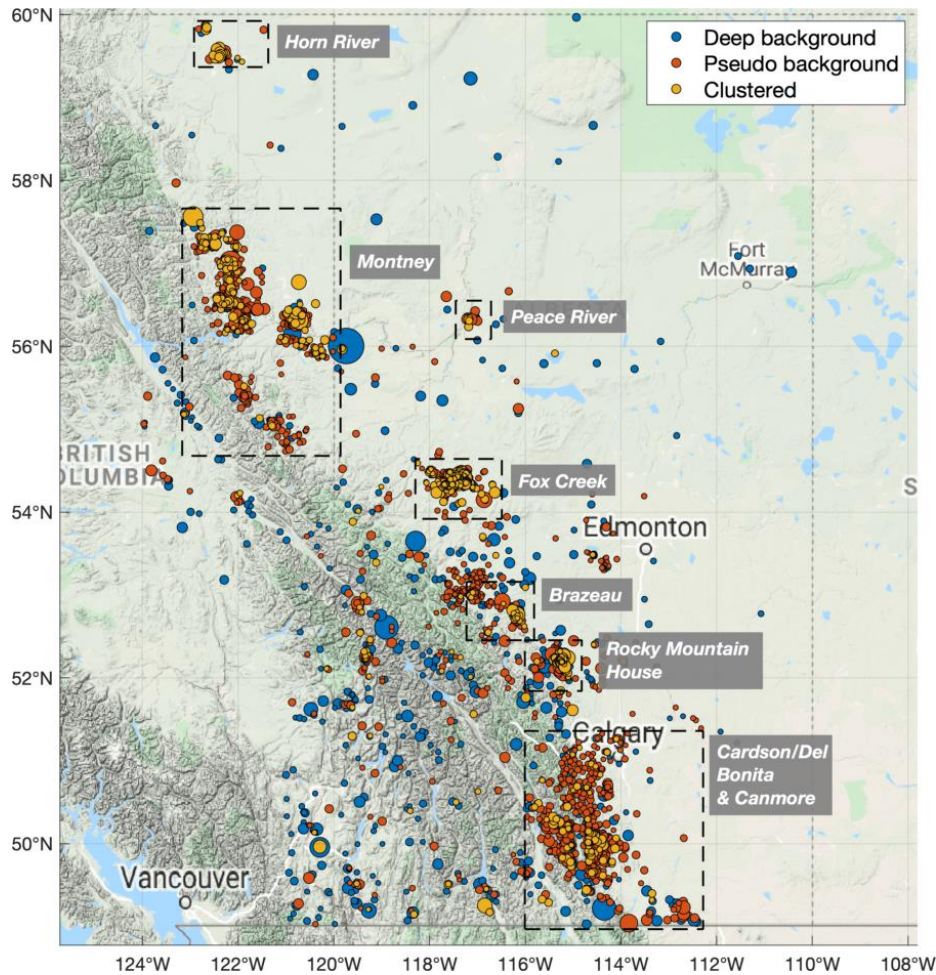


455

456 *Figure 3: Joint (T,R) distributions of individual modes for the regional WCSB catalogue (1975-2018) using  $M_0 = 2.0$ . Colour*  
 457 *bar indicates frequency of inter-event distance occurrence. Bold white line indicates the threshold  $\log_{10} \eta_{\text{thresh}}$  between tightly*  
 458 *clustered and loosely clustered components. Thin white line indicates the threshold  $\log_{10} \eta_{\text{tect}}$  between loosely clustered and*  
 459 *deep background components. a) Entire distribution. b) Tightly clustered mode. c) Loosely clustered mode. d) Deep background.*

460 Figure 3 plots the modal decomposition of the joint distribution, where each  
 461 subpopulation is plotted separately, removing the dependence on mixing proportion. As  
 462 mentioned above, if a distribution does not intensify along the bisecting diagonal (constant  $\eta$ )  
 463 and instead forms an elliptical cloud, then a trend may exist in the data as a deviation from  
 464 Poisson behavior. As expected, the tightly clustered subpopulation deviates substantially from  
 465 the diagonal and forms an ellipse within the sub-region  $\{-5 < \log_{10} T < -3.5 \mid -1.5 <$   
 466  $\log_{10} R < -0.5\}$ . The loosely clustered mode is faintly concentrated along the diagonal yet also  
 467 forms a cloud within the sub-region  $\{-3.5 < \log_{10} T < -1 \mid -1.5 < \log_{10} R < 1\}$ . By contrast,

468 the deep background is distributed very closely along the diagonal and stretches almost its  
 469 complete length, most clearly resembling a Poisson process.



470

471 **Figure 4:** Spatial map of earthquakes for the regional WCSB catalogue (1975-2018) using  $M_0 = 2.0$ , represented in terms of  
 472 their nearest-neighbour distance categorization. Blue markers are the deep background, orange markers are the loosely  
 473 clustered events and yellow markers are the tightly clustered events. Marker size indicates magnitude. Dashed boxes surround  
 474 areas of suspected induced clustering (see (Atkinson et al., 2016)).

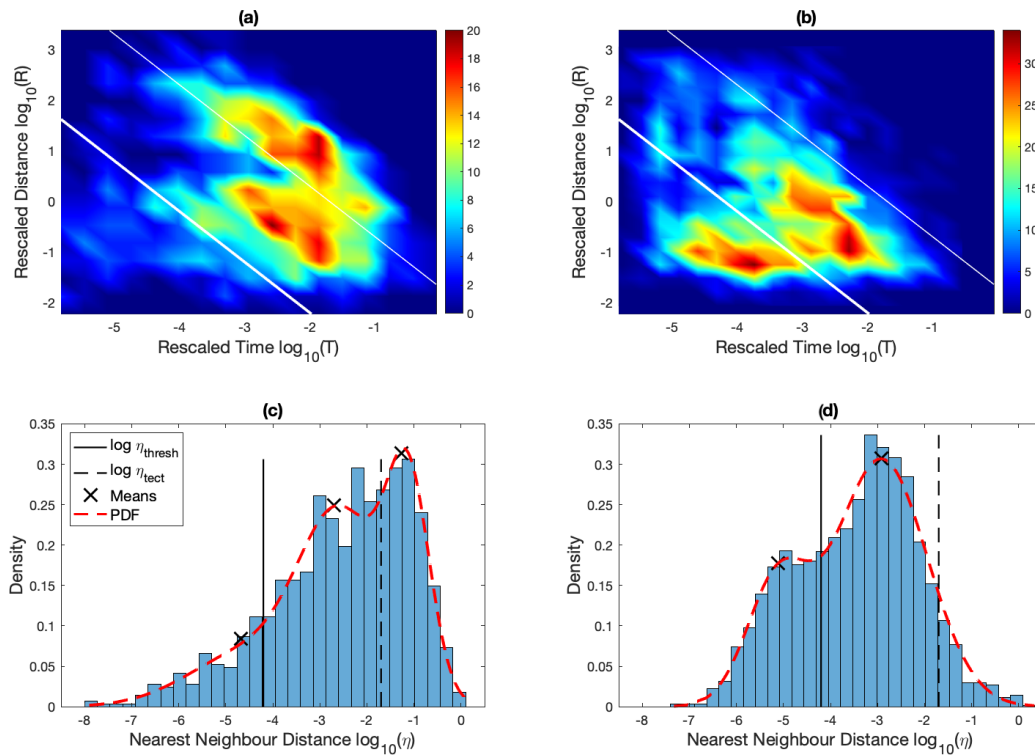
475 A spatial map of the catalogued earthquakes is displayed in Figure 4. Blue markers  
 476 represent deep background events, while orange and yellow markers represent the loosely  
 477 clustered and tightly clustered events, respectively. Dashed boxes surround individual areas of  
 478 suspected induced activity. According to the NND method, both the blue and orange markers are  
 479 classified as the “background” portion of events. However, the two subpopulations are not  
 480 representative of the same type of seismicity. As a physical representation of the results in Figure  
 481 3, the blue markers are substantially more evenly distributed and seemingly reflective of the

482 natural tectonic background (the majority occur along the foreland belt of the Rocky Mountain  
483 range), whereas an obvious spatial dependence on the distribution of orange and yellow markers  
484 is indicative of clustering. The orange and yellow markers overwhelmingly dominate the dashed  
485 boxes.

486 We also observe that the background events which occurred farther away from their own  
487 potential parent were less likely to initiate a clustering sequence, with deep background events  
488 substantially less likely to trigger future earthquakes than loosely clustered events. Out of 320  
489 non-single event families, 281 (88%) began from the loosely clustered mode and 39 (12%) began  
490 from the deep background. Out of the 35 identified *significant* sequences, which we arbitrarily  
491 define as containing five or more events, 33 (94%) initiated from loosely clustered ancestors  
492 while only 2 (6%) initiated from the deep background. This correlation holds for all family sizes;  
493 as the number of events within a family *increases*, the likelihood of the family to originate from  
494 the loosely clustered mode also *increases*. On the other hand, it is true that there is a larger  
495 population of loosely clustered events, which could partially explain the disparity. However,  
496 even relative to the mixing proportion of each mode, a non-single event family is twice as likely,  
497 and a significant event family is nearly four times as likely to have originated from the loosely  
498 clustered mode rather than in the deep background. This may be observed in Figure 4; overlap  
499 occurs substantially between loosely clustered (orange) and tightly clustered (yellow) markers,  
500 but rarely occurs between deep background (blue) and tightly clustered (yellow) markers.  
501 Overall, the differences between the loosely clustered and deep background subpopulations  
502 appear noteworthy and demonstrable.

503

## 4.2 Separated Time Periods: 1975-2009 and 2010-2018



504

505 *Figure 5: Comparison of NND distributions of the regional WCSB catalogue across time using  $M_0 = 2.0$ . (a,b) Joint*  
 506 *distributions of the temporal and spatial components ( $T,R$ ). Bold white line indicates the threshold  $\log_{10} \eta_{\text{thresh}}$  between tightly*  
 507 *clustered and loosely clustered components. Thin white line indicates the threshold  $\log_{10} \eta_{\text{tect}}$  between loosely clustered and*  
 508 *deep background components. Colour bar indicates frequency of occurrence. (c,d) Normalized densities of  $\eta$  values. Solid black*  
 509 *line is  $\log_{10} \eta_{\text{thresh}}$  and dashed black line is  $\log_{10} \eta_{\text{tect}}$ . Dashed red line is the normalized probability density function of the*  
 510 *Gaussian mixture and black crosses are the component means. (a, c) 1975-2009, both background modes are dominant. (b, d)*  
 511 *2010-2018, deep background shrinks while tightly clustered mode appears. The loosely clustered subpopulation is common to*  
 512 *both time frames.*

513 Figure 5 presents the  $(T,R)$  and  $\eta$  distributions of the WCSB for separated time intervals.  
 514 From 1975-2009, the regional catalogue is characterized by natural activity and isolated cases of  
 515 induced clustering due to conventional oil and gas production and associated wastewater  
 516 disposal, primarily within the Duvernay and Montney formations (Wetmiller, 1986; Rogers &  
 517 Horner, 1991; Horner et al., 1994; Baranova et al., 1999; Schultz et al., 2014). The resulting  
 518 space-time inter-event distance distribution shows that both background modes are dominant,  
 519 containing 83% of all events analyzed, indicating mainly single events and loose clustering, but  
 520 little tight clustering (Figure 5a and Figure 5c). In contrast, the regional catalogue between 2010-  
 521 2018 is characterized by sparse natural activity, due to the shorter time-frame, and large amounts

522 of induced activity attributed to the sharp rise in the implementation of horizontally drilled HF  
523 operations within the Duvernay, Montney, Cardium and Bakken formations, among others (B.C.  
524 Oil and Gas Commission, 2012, 2014; Schultz, Mei, et al., 2015; Schultz, Stern, Novakovic, et  
525 al., 2015; Atkinson et al., 2016; Bao & Eaton, 2016). The joint distribution changes strikingly;  
526 the deep background subpopulation nearly disappears and a tightly clustered mode arises,  
527 indicating both substantial loosely clustered and tightly clustered seismicity (Figure 5b and  
528 Figure 5d). An important factor to consider is the variation in seismic monitoring capability over  
529 time; many more stations were operational during the recent time period, which undoubtedly had  
530 an effect on the distributions. We show below that the changes in mixing proportion across time  
531 are vastly disproportionate and cannot be entirely attributed to improvement in network  
532 detection.

533 The Gaussian mixture model analysis over the first time period detects the same three  
534 modes identified over the entire time frame. Over the second period, it picks out only the tightly  
535 clustered and loosely clustered components. This is understandable, as the deep background  
536 shrinks and ultimately contains only 7.5% of the mixing proportion from 2010-2018. Overall,  
537 there is a 27% drop in the relative number of deep background events and a 10% increase in the  
538 proportion of loosely clustered events between the two time periods. There is a 17.5% increase in  
539 the relative population of tightly clustered events. The changes in rate are disproportionate; while  
540 the yearly detected  $M_{2+}$  deep background rate roughly doubles, the loosely and tightly clustered  
541 rates increase tenfold and seventeen-fold, respectively. The disproportionality holds above the  
542 estimated regional completeness level  $M_c = 3.0$ ; for magnitudes above this threshold, the deep  
543 background rate is almost doubled across the two time periods, while the loosely and tightly  
544 clustered rates both increase nearly six-fold (Figure S8). We perform a two-sample Kolmogorov-  
545 Smirnov test on the distributions of  $\eta$  values between the separated time periods, in order to test  
546 the null hypothesis that the differences observed are within sampling errors and the two samples  
547 are actually from the same continuous distribution. The test rejects the hypothesis at the 99%  
548 confidence level.

549 These results suggest that the changes in the inter-event distance distribution across  
550 Alberta and eastern B.C. over time are statistically significant and not naturally occurring. The  
551 decreased mixing proportion of deep background events indicate that the majority of the recent  
552 seismicity is not tectonic, while the increase in tightly clustered seismic activity correlates

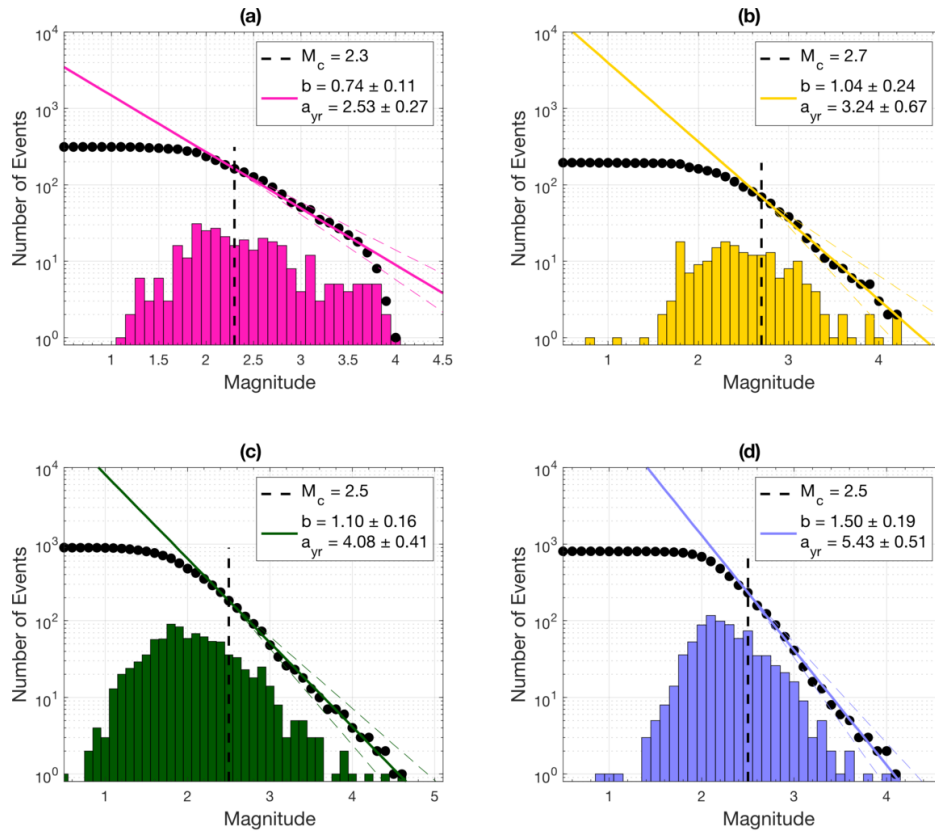
553 temporally with the rise in horizontally drilled HF treatments within the region. Figure 4 shows  
554 that clustering is highly spatially correlated with human activity as well, with smaller inter-event  
555 distances (i.e. orange and yellow markers) transpiring chiefly near areas flagged as suspicious.  
556 The statistical properties of several of these suspicious areas are explored in detail in the next  
557 section.

## 558 **5 Analysis and Comparison of Isolated Seismic Clusters**

559 Here we examine four separate cases of seismic clustering within the Western Canada  
560 Sedimentary Basin (WCSB): the Rocky Mountain House cluster (RMHC) – induced by  
561 conventional natural gas extraction, the Montney clusters (MC1 and MC2) – triggered by  
562 wastewater disposal and hydraulic fracturing, and the Fox Creek Cluster (FCC) – induced by  
563 hydraulic fracturing (these clusters are described in more detail in section 2; see Figures S1-4 for  
564 related event maps).

565

## 5.1 Frequency-Magnitude Statistics



566

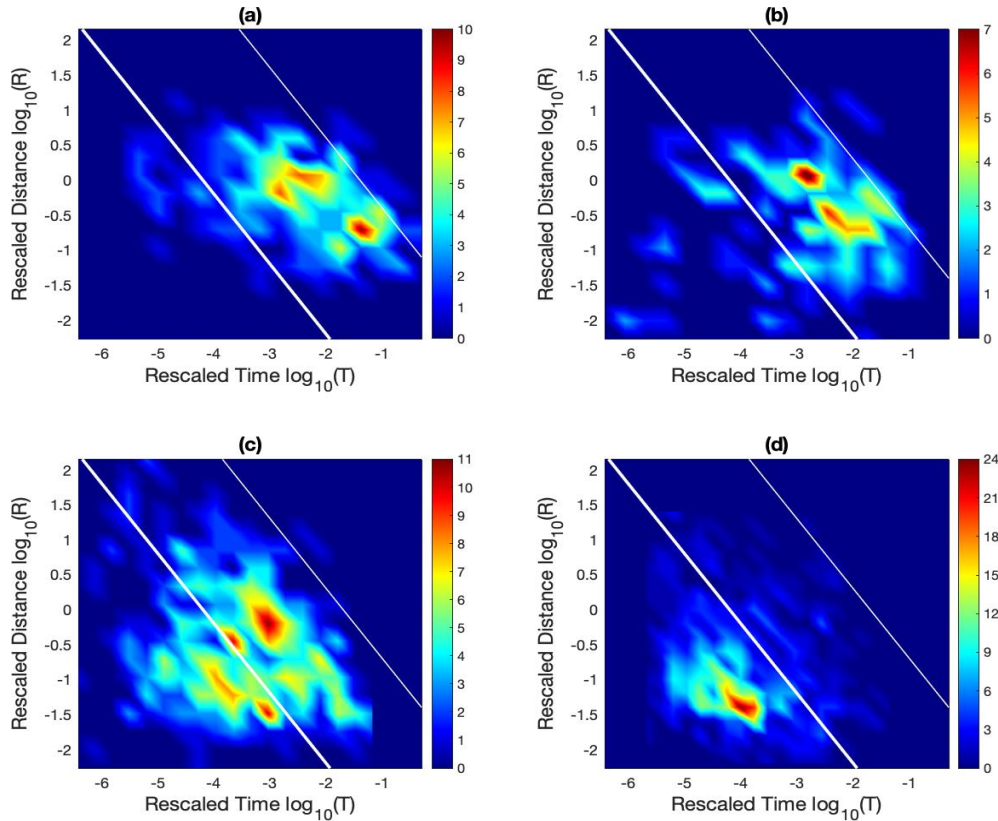
567 **Figure 6:** Frequency-magnitude distributions and estimated Gutenberg-Richter parameters for each investigated cluster.  
 568 Coloured histograms represent the non-cumulative magnitude distributions and black dots represent the cumulative magnitude  
 569 distributions. Dashed black lines indicate the determined magnitude of completeness. Coloured lines represent the modeled GR  
 570 relations. a) Rocky Mountain House cluster. b) Montney cluster 1. c) Montney cluster 2. d) Fox Creek cluster.

571 We begin by assessing the frequency-magnitude distributions (FMDs) of each cluster and  
 572 computing their Gutenberg-Richter scaling parameters (Figure 6). The FMD plots the cumulative  
 573 and non-cumulative frequencies of earthquake magnitude occurrence in log-linear space. We use  
 574 the maximum likelihood method to determine the  $b$ -values along with their 95% uncertainties  
 575 (Aki, 1965; Utsu, 1966; Shi & Bolt, 1982). The local completeness level in each case was  
 576 determined using a suite of catalogue-based methods, namely the method of maximum curvature,  
 577 the goodness-of-fit test, and the method of  $b$ -value stability (Wiemer & Wyss, 2000; Cao & Gao,  
 578 2002).

579 The RMHC, which was induced by conventional gas extraction, is characterized by a  
 580 very broad distribution of event magnitudes resulting in a very low  $b$ -value (Figure 6a,  $b =$

581  $0.74 \pm 0.11$ ). This contrasts with the Fox Creek cluster (FCC), induced by hydraulic fracturing,  
 582 whose FMD is very steep and contains many more small magnitude events and fewer large  
 583 magnitude events. As a consequence, it is described by a very high  $b$ -value (Figure 6d,  $b =$   
 584  $1.50 \pm 0.19$ ). Both the wastewater disposal and hydraulic fracturing-induced Montney clusters  
 585 (MC1 and MC2) have more typical magnitude distributions (Figure 6b,  $b = 1.04 \pm 0.24$  and  
 586 Figure 6c,  $b = 1.10 \pm 0.16$ ). The  $a$ -values are normalized to reflect the yearly-detected  
 587 seismicity rate. It is unsurprising that the more recent, densely populated clusters (MC2 and  
 588 FCC) have the highest yearly  $a$ -values, whereas the RMHC and MC1 both span longer periods of  
 589 time and are smaller overall, resulting in lower yearly  $a$ -values.

## 590 5.2 Nearest-Neighbour Distance Distributions



591

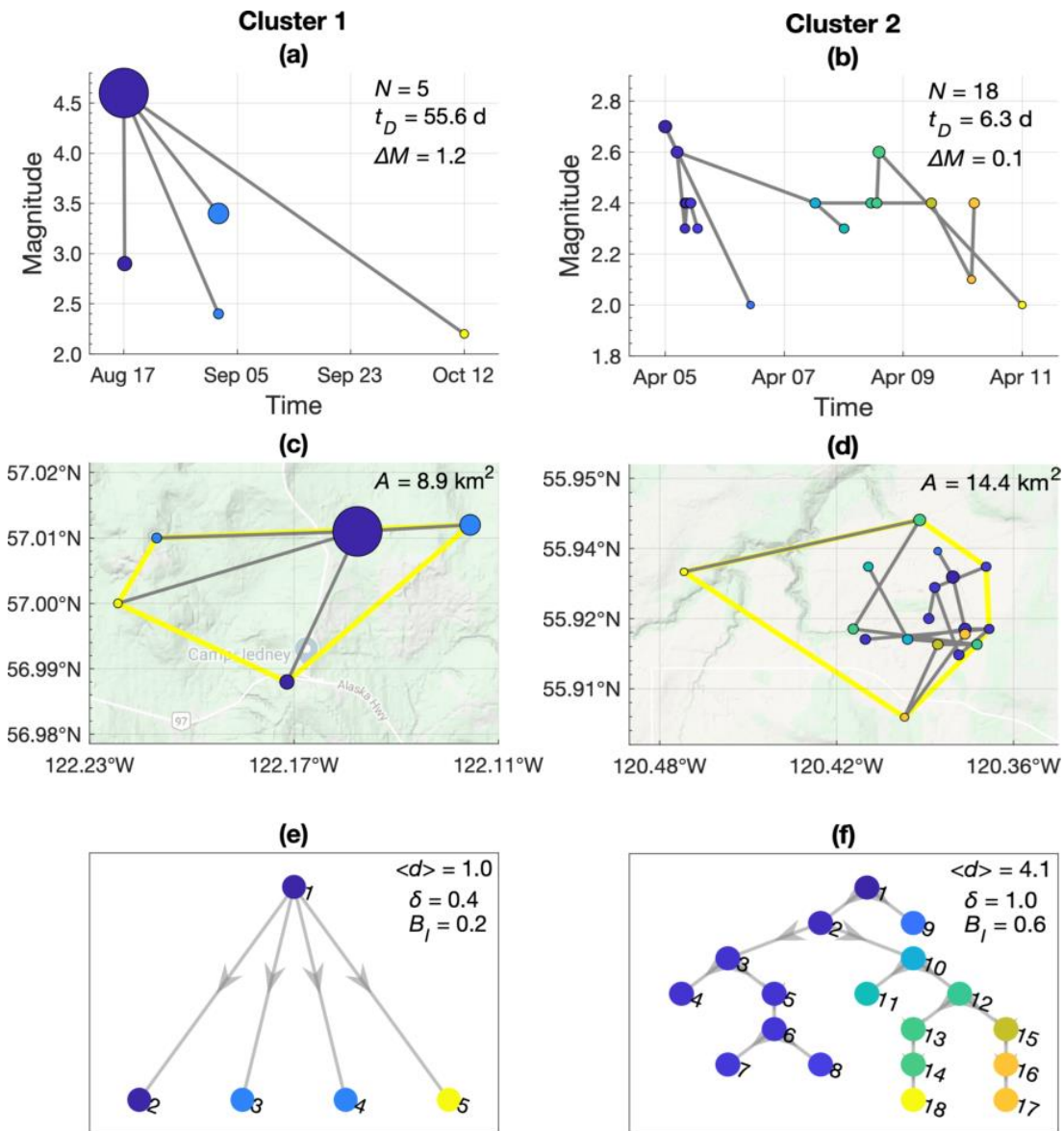
592 **Figure 7:** Joint NND distributions of the temporal and spatial inter-event distances ( $T,R$ ) for each investigated cluster. Bold  
 593 white line indicates the threshold  $\log_{10} \eta_{thresh}$  between tightly and loosely clustered components. Thin white line indicates the  
 594 threshold  $\log_{10} \eta_{tect}$  between the loosely clustered and deep background. Colour bar reflects inter-event distance occurrence  
 595 frequency. a) Rocky Mountain House cluster. b) Montney cluster 1. c) Montney cluster 2. d) Fox Creek cluster.

596 Next, we use the  $b$ -values determined above to parameterize and plot the joint space-time  
 597 nearest-neighbour distance (NND) distributions for each cluster, which reflect the mixing  
 598 proportions of loosely and tightly clustered earthquakes (Figure 7). As an initial observation, the  
 599 modal locations of all four clusters provide confirmation of some of the regional interpretations  
 600 formed in section 4. In particular, we suggested that the regional clustering observed within the  
 601 WCSB occurred within a distinct subset of the multidimensional inter-event NND space, namely  
 602 within the  $\log_{10} \eta \leq \log_{10} \eta_{tect}$  realm (i.e. within the loosely and tightly clustered domains). The  
 603 remaining earthquakes were evenly distributed and occurred largely within the  $\log_{10} \eta >$   
 604  $\log_{10} \eta_{tect}$  realm (i.e. within the deep background domain). From Figure 7, it is indeed the case  
 605 that all of the investigated clusters occupy the  $\log_{10} \eta \leq \log_{10} \eta_{tect}$  realm.

606 However, *within* the  $\log_{10} \eta \leq \log_{10} \eta_{tect}$  realm, several distinctions between the clusters  
 607 regarding their mixing proportions can be made. The RMHC (Figure 7a) and MC1 (Figure 7b)  
 608 distributions are visually similar, containing dominant populations of loosely clustered events.  
 609 We can estimate the proportions of loosely clustered background events  $\mu_{GMM}$ , based on a  
 610 bimodal Gaussian mixture model (disregarding the deep background), which is computed as a  
 611 fraction of the total seismicity within each cluster. This yields  $\mu_{GMM} = 0.86$  for the RMHC and  
 612  $\mu_{GMM} = 0.74$  for the MC1. The majority of earthquakes in these clusters occur somewhat closely  
 613 together in space and time, but mainly as separate instances that rarely trigger future earthquakes.  
 614 This loosely clustered activity of single events may reflect the type of seismicity expected to  
 615 occur within the WCSB due to steady, long-term alterations to the subsurface stress field, such as  
 616 long-term gas extraction and wastewater disposal (Wetmiller, 1986; Horner et al., 1994;  
 617 Baranova et al., 1999; B.C. Oil and Gas Commission, 2014). Conversely, both the MC2 (Figure  
 618 7c) and FCC (Figure 7d) distributions contain distinct modes within the tightly clustered  
 619 ( $\log_{10} \eta < \log_{10} \eta_{thresh}$ ) domain. The existence of these modes indicates that a significant  
 620 proportion of earthquakes are occurring very closely together and are possibly occurring in direct  
 621 response to a triggering mechanism (previous earthquakes and/or external forces). The  
 622 proportion of loosely clustered events in the MC2, estimated by the bimodal Gaussian mixture  
 623 model, reduces to  $\mu_{GMM} = 0.41$ . The FCC is further distinguishable from the other clusters by its  
 624 apparent lack of a loosely clustered subpopulation ( $\mu_{GMM} = 0.09$ ). This is quite significant, as it  
 625 implies that either: (i) the small population of background events occurring in this area is capable  
 626 of triggering massive amounts of tightly clustered activity; or (ii) other, external triggering

627 factors are contributing to the unnatural levels of event sequencing. Based on the spatiotemporal  
 628 correlations between the increased rates of seismicity and the rise in horizontally drilled HF  
 629 operations made here and in other studies, it is logical to connect HF as one of the probable  
 630 causative mechanisms (discussed further below).

631 **5.3 Event-Family Classification**



632  
 633 **Figure 8:** Characterizations of “burst” and “swarm” sequences found in the MC2. Circles represent earthquakes and are  
 634 coloured chronologically from darkest to lightest; grey lines represent the strong links connecting them. (a,b) Event family  
 635 magnitudes vs. times of occurrence.(c,d) Spatial maps of events; yellow border outlines the hull area occupied by the sequence.  
 636 (e,f) Topological trees, which branch downward in time.

637 In this subsection, we discretize each of the RMHC, MC1, MC2, and FCC's tightly  
 638 clustered NND subpopulations into hierarchical families based on the strong links between  
 639 parents and offspring events. We then categorize these families as aftershock sequences, seismic  
 640 swarms, a combination of the two, or neither, based on statistical parameters outlined by Zaliapin  
 641 & Ben-Zion (2013b) (see section 3.3 for a detailed description of these parameters). We consider  
 642 only those families consisting of three or more events; event-pairs are discarded, as are the single  
 643 events that chiefly populate the background mode.

644 The RMHC and MC1 are each composed of six significant sequences across 26-year  
 645 periods; these sequences are small, with the largest containing five and eight events, respectively.  
 646 The MC2 is composed of ten families over a 9-year period, the largest containing 17 events,  
 647 while FCC is comprised of 16 sequences over a 6-year period, the largest containing 80 events.  
 648 Figure 8 shows examples of two families identified in the MC2, along with their associated  
 649 parameters, displayed as time-magnitude sequences, spatial maps and time-oriented, topological  
 650 trees. Cluster 1 is a typical aftershock sequence while Cluster 2 is a swarm. Intuitively, Cluster 1  
 651 is characterized by a *burst* or *spray-like* shape, involving a dominant mainshock causing several  
 652 lower magnitude, 1<sup>st</sup> generation offspring in multiple directions. Conversely, Cluster 2 displays a  
 653 *linear* or *path-like* shape where the events are chained together gradually, the mainshock is less  
 654 distinct and is succeeded by multiple generations of aftershocks.

655 *Table 1: Mean and median parameter values for all significant event families within each investigated cluster.*

Cluster	Number of Families		N	$\langle d \rangle$	$\delta$	$B_I$	$A$ (km <sup>2</sup> )	$t_D$ (days)	$\Delta M$
RMHC	6	Mean	3.67	1.22	0.64	0.50	8.40	1.33	0.57
		Median	3.5	1	0.58	0.5	5.93	1.00	0.25
MC1	6	Mean	4.17	1.83	0.92	0.68	23.45	23.60	0.35
		Median	3.5	2	0.855	0.58	4.42	5.52	0.25
MC2	10	Mean	7.60	2.76	1.08	0.67	26.33	24.83	0.27
		Median	5.5	3	1.125	0.71	7.19	5.23	0.1
FCC	16	Mean	27.13	7.60	1.54	0.66	20.97	32.09	0.22
		Median	20.5	6.19	1.27	0.65	17.16	15.05	0.1

656 Table 1 presents the mean and median parameter values for all of the detected sequences  
657 (see Figures S9-12 for the structural representations of all sequences, analogous to Figure 8). The  
658 RMHC is almost entirely composed of small bursts; these sequences have a relatively large  
659 mainshock and are followed by few (four or less) aftershocks. The mean and median values of  
660 the magnitude differential  $\Delta m$  are large while the normalized leaf depth  $\delta$  and inverted  
661 branching number  $B_I$  are small, highlighting the spray-like nature of the sequences. The MC1 is  
662 comprised of a mixture of small bursts and swarms. Its mean and median  $\Delta m$  are slightly smaller  
663 and its topological parameters are larger than the RMHC's, indicating more swarm-like behavior  
664 and possibly some level of inter-event triggering. The MC2 is more swarm-like than the MC1; it  
665 consists of a large swarm, a large burst and smaller sequences. The mean and median topological  
666 parameters are larger than both previous clusters while the magnitude differential is smaller. This  
667 signifies that, apart from the large burst, the mainshocks are generally less distinct, the sequences  
668 are graphically deeper and there are more parent events and fewer leaves. The mean  $\Delta m$  is  
669 skewed somewhat by the large burst, which explains the disparity between it and the median  
670 value. The FCC is overwhelmingly swarm-like; 13 of the 16 sequences are chain-like in time  
671 (mean and median  $\delta$  are large) and contain similarly sized events (mean and median  $\Delta m$  are  
672 small). The  $B_I$  values are similar to the MC1 and MC2. The remaining 3 families in the FCC  
673 consist of a large burst and two swarm-bursts (where there is a large mainshock but also many  
674 generations of foreshocks and aftershocks chained together; see Figure S12, clusters 5 and 6). It  
675 is important to note that while the average leaf depth  $\langle d \rangle$  scales with the sequence size  $N$ , both  $\delta$   
676 and  $B_I$  do not.

677 The spatial extents  $A$  and timeframes  $t_D$  are slightly more difficult to contextualize as  
678 these parameters scale with  $N$ . The sequences within the RMHC are quite consistent; they all  
679 cover small spatial areas and decay rapidly (within days). The MC1 suffered from occasional  
680 improper location recording, where several events were placed in the same spot, resulting in  
681 inaccurate area calculations. Its time periods are variable; the two largest families are bursts and  
682 persist for over a month while the remaining smaller sequences degenerate within days. The  
683 MC2 is consistent apart from a large burst, which covers a large area and persists for several  
684 months. The remaining sequences are much more constrained spatiotemporally, including a large  
685 swarm sequence, which explains the disparity between mean and median  $A$  and  $t_D$  values.  
686 Finally, the FCC's swarm sequences are similar, with comparable  $A$  and  $t_D$  values. The largest

687 families cover spatial areas between 30-50  $km^2$  and span approximately a month's time, while  
 688 the smaller ones cover 10  $km^2$  or less and decay within two weeks. The lone identified burst  
 689 sequence in the FCC occupies a comparable area but spans over half a year's time (Figure S12,  
 690 cluster 4).

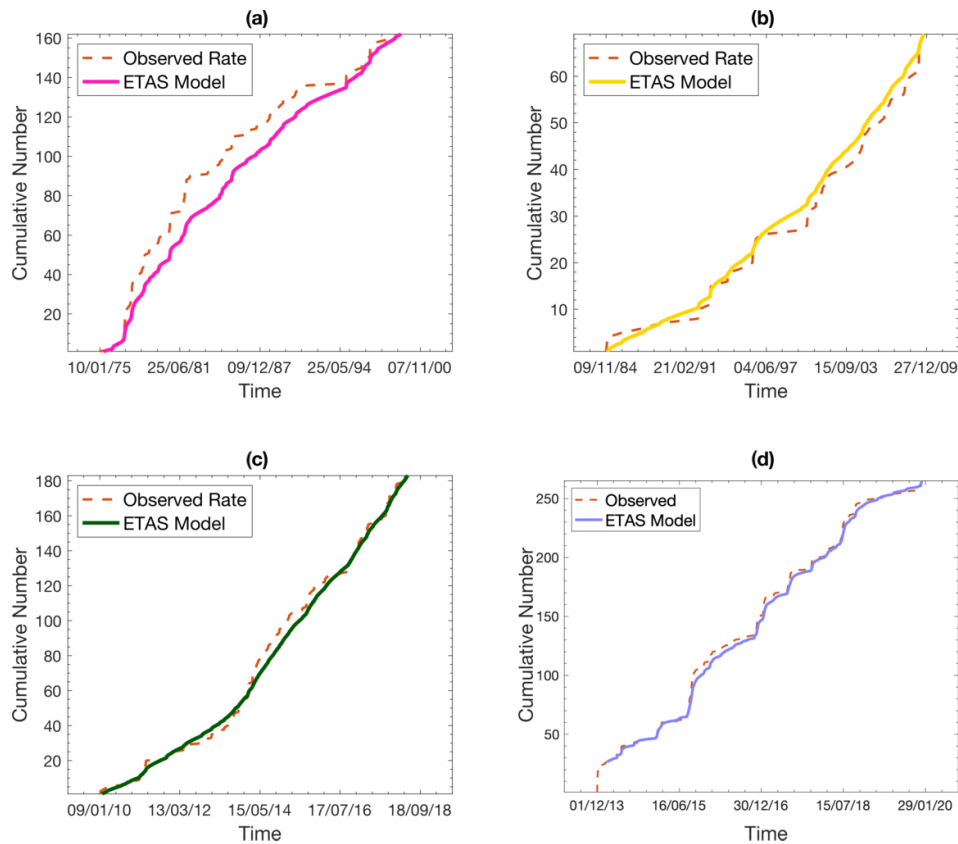
#### 691 5.4 The Epidemic Type Aftershock Sequence Model

692 Finally, we use the point-process epidemic-type aftershock sequence (ETAS) model to  
 693 compare the rates of seismicity, aftershock parameters and model-fitting quality between the four  
 694 clusters. The ETAS model, developed by Ogata (1988, 1989), is a stochastic branching model  
 695 based on an extension of the Omori-Utsu law of aftershocks (Omori, 1894; Utsu, 1961). It aims  
 696 to represent the seismicity rate as the summation of a constant background term and a  
 697 parameterized aftershock kernel. The rate is modeled as a function of previous activity; at time  $t$ ,  
 698 it is conditioned by all events  $M_i$  that satisfy  $t_s \leq t_i < t$ , where  $t_s$  is the start of a target window.  
 699 According to the model, each seismic event has the potential to trigger its own aftershock  
 700 sequence. Given the completeness magnitude  $M_c$ , the earthquake rate  $\lambda$  at time  $t$  is

$$\lambda(t|H_t) = \mu + \sum_{t_i < t} \frac{K e^{\alpha(M_i - M_c)}}{\left(\frac{t - t_i}{c} + 1\right)^p}, \quad [8]$$

701 where  $H_t$  is the conditional earthquake occurrence history prior to time  $t$  within the target  
 702 window.  $\mu$  represents the independent background rate,  $K$  is the aftershock productivity,  $p$   
 703 controls the observed power law-based rate of aftershock decay, and  $c$  is the time offset between  
 704 the mainshock and start of decay. The parameter  $\alpha$  governs the degree of aftershock cascading  
 705 for a given magnitude. Larger values of  $\alpha$  imply a greater sensitivity to magnitude in the  
 706 generation of aftershocks, which has been observed for great earthquakes (Ogata, 1992; Omi et  
 707 al., 2014). Conversely, smaller  $\alpha$  values reduce the significance of event magnitude on aftershock  
 708 triggering. This characteristic has been linked to swarm sequences where mainshocks are less  
 709 distinct (Mogi, 1963; Utsu, 1970; Ogata, 1988). Estimation of the set of parameters  $\varphi =$   
 710  $\{\mu, K, \alpha, c, p\}$  may be obtained by maximizing the log-likelihood function for  $\lambda(t)$  (see Ogata,  
 711 1989).

712 The quality of the ETAS model fit is generally evaluated based on a transformation of  
 713 occurrence times, where a new set of times  $\tau$  is defined such that  $\tau_i$  is the cumulative conditional  
 714 intensity function at time  $t_i$ . A plot of the cumulative ETAS model rate versus the transformed  
 715 time thus results in an increasing function with constant unit slope. If the model fits the data  
 716 well, then a plot of the observed cumulative event count versus the transformed time will match  
 717 the cumulative model with rate close to unity. We determine the model's quality-of-fit (*QOF*) to  
 718 each cluster by quantifying the deviations of the observed cumulative plot from the ideal  
 719 function in transformed time; the *QOF* value is computed as the normalized area present between  
 720 the two plots. The maximum area value is 0.5, corresponding to the worst possible fit to the  
 721 sequence; a value closer to 0 implies a better fit.



722  
 723 **Figure 9:** ETAS Models in original time for each investigated cluster. Dashed orange lines are the observed cumulative rates of  
 724 seismicity. Solid coloured lines are the optimized models. Dates are given in dd/mm/yy format. a) Rocky Mountain House cluster.  
 725 b) Montney cluster 1. c) Montney cluster 2. d) Fox Creek cluster.

726 Figure 9 presents the ETAS model and observed seismicity rates for each cluster, using  
 727 events above the magnitude of completeness thresholds determined in subsection 5.1. The

728 corresponding background and aftershock parameters are provided in Table 2. The model  
 729 successfully converged for the RMHC, MC1, and MC2 but failed to converge to realistic  
 730 parameter values for the FCC. We therefore constrained the background rate parameter  $\mu$  to  
 731 nearly zero and reran the simulation, achieving convergence and an improved *QOF*. Justification  
 732 for this approach is provided below. The *QOF* varies for each cluster. The RMHC (Figure 9a) is  
 733 by far the worst fit; the model underpredicts the rate across the entire time frame. The MC1  
 734 (Figure 9b) fit is fair; this time, the model slightly overpredicts the rate. The MC2 (Figure 9c) is  
 735 fit well, while the FCC (**Figure 9d**, fixed  $\mu$ ) is fit very well. The type of seismicity within each  
 736 cluster, as illustrated by the NND model in the previous subsections, may provide some  
 737 explanation for the differing *QOFs*. The FCC is composed of large, distinct clustering sequences  
 738 that are easily distinguishable across time. The ETAS model appears to be correctly modeling  
 739 these individual spikes in the rate. Conversely, the RMHC is composed of a loosely clustered  
 740 type of seismicity that produces few clearly defined sequences and mainly manifests as elevated  
 741 background activity. Consequently, the ETAS model may have encountered difficulty in  
 742 replicating the gradually increasing rate with an absence of aftershock sequences. The steady  
 743 RMHC rate may be more suitably modeled by an increased background parameter  $\mu$  without the  
 744 aftershock kernel. The improved *QOF* of the MC2 over the MC1 could be further evidence that  
 745 the ETAS model requires defined sequences with which to optimize its fit, although the MC1  
 746 dataset is likely too small for a realistic comparison.

747 *Table 2: ETAS model parameters for each investigated cluster.*

<b>Cluster</b>	$M_c$	$N$	$\mu$	$K$	$c$	$p$	$\alpha$	<i>QOF</i>
<b>RMHC</b>	2.3	162	0.0047	0.26	0.24	1.06	0.76	0.072
<b>MC1</b>	2.7	69	0.0033	3.09	0.0019	0.81	0.84	0.042
<b>MC2</b>	2.5	183	0.016	1.0	0.022	0.84	0.39	0.020
<b>FCC*</b>	2.5	242	0.000002	0.42	0.62	1.25	0.47	0.017

\*  $\mu$  is held constant.

748 It is problematic to compare the parameter values between all the clusters, as the model  
 749 may not be accurately representing the rate in the cases of the RMHC and MC1. For the MC2  
 750 and FCC, the ETAS model seems able to accurately capture the swarm activity in addition to the

751 aftershock sequences for which it was intended. 21 out of the 26 event sequences identified  
752 within the MC2 and FCC do not have distinct mainshocks but are instead composed of similarly  
753 sized events. This appears to be reflected in the optimized ETAS  $\alpha$  parameter, which governs the  
754 dependence on magnitude in the generation of aftershocks.  $\alpha$  is low for both clusters, indicating  
755 that the model may be correctly identifying the persistent nature of the swarm sequences, which  
756 continue to produce generations of offspring despite the lack of an obvious mainshock. The  $p$   
757 parameter, which controls the sequence decay rate, is low for the MC2 and high for the FCC.  
758 This might again be attributable to the more gradual rate increase within the MC2 (Figure 9c)  
759 compared to the sharp spikes due to the large, tightly constrained sequences observed within the  
760 FCC (Figure 9d).

761 Finally, within the FCC, a better fit and a realistic convergence are achieved by  
762 constraining the background rate  $\mu$ . Generally, the ETAS  $\mu$  parameter is optimized to represent  
763 independent seismicity as a non-zero constant, which allows for the generation of the conditional  
764 aftershock rate. Consequently,  $\mu$  may relate to the nearest-neighbour loosely clustered  
765 subpopulation, as they both represent the subset of background earthquakes occasionally  
766 preceding clustered activity. While the three other investigated clusters contained high amounts  
767 of loosely clustered activity, likely resulting from long-term stress perturbations caused by fluid  
768 extraction and injection, the FCC is comprised of tightly clustered sequences and relatively few  
769 background events. This suggests that external factors may be contributing directly to the  
770 triggering of seismicity. The absence of the loosely clustered population was used as motivation  
771 for the fixed  $\mu \approx 0$  constraint. When  $\mu$  was similarly fixed on a trial basis for the other clusters,  
772 either the QOF was worse or the model did not converge. This does make sense, as the  
773 seismicity in those areas is largely made up of an elevated background with few significant  
774 sequences, and so assuming an absence of background seismicity would be inaccurate. The  
775 comparatively high-quality fit of the model to the FCC also provides some confirmation that the  
776 ETAS model seems to perform better on a dataset containing separable, tightly connected  
777 sequences. For seismic clusters resembling an elevated background rate, on the other hand, it  
778 may not be able to predict what events are or are not part of an earthquake sequence.

779 **6 Discussion**

780 Many regional studies of anthropogenic seismicity have described an elevation in  
781 background seismicity during and immediately after potential earthquake-inducing processes  
782 such as geothermal energy production, wastewater disposal, hydraulic fracturing etc. (Lombardi  
783 et al., 2010; Llenos & Michael, 2013; Schoenball et al., 2015; Maghsoudi et al., 2016; Zaliapin  
784 & Ben-Zion, 2016; Schoenball & Ellsworth, 2017; Martínez-Garzón et al., 2018). In sections 4  
785 and 5, we found evidence that an induced background subpopulation of earthquakes in the  
786 WCSB was elevated near areas of human activity, which could be separated from the tectonic  
787 rate in the nearest-neighbour distance (NND) distributions. This elevated background was more  
788 specifically a collection of earthquakes that was loosely clustered in certain areas over limited  
789 time frames; its inter-event space-time distances were measurably lower than the regional  
790 Poisson-like background but larger than typical clustering activity. This is likely to have been the  
791 case in other regions as well. For example, Zaliapin & Ben-Zion (2016) used the NND method to  
792 examine seismicity within selected regions across the state of California; these regions were  
793 either (i) dominated by induced activity related to geothermal operations, (ii) a mixture of  
794 tectonic and induced earthquakes, or (iii) characterized entirely by tectonic events. In every  
795 instance, the anthropogenic seismicity contained a background mode that was situated much  
796 closer to the clustered mode than the natural activity. The separation threshold value between  
797 subpopulations was smallest for type (i) areas and largest for areas of type (iii); this difference  
798 spanned several orders of magnitude. Similar observations were made by Schoenball et al.  
799 (2015), who assessed the seismicity surrounding and within the Coso geothermal field in  
800 southern California. The induced seismicity again contained a background element positioned  
801 closer to the clustered mode compared to the surrounding earthquakes, which were attributed to  
802 tectonic and magmatic sources. Interestingly, the background mode held a dominant mixing  
803 proportion during the coproduction intervals and also extended further downward along the  
804 diagonal towards larger  $T$  and smaller  $R$ , suggesting that a large proportion of the induced  
805 activity was acting as an elevated Poisson process of independent events. Vasylykivska & Huerta  
806 (2017) studied the rapidly increasing earthquake rate in Oklahoma associated with large-scale  
807 wastewater injection. During the pre-injection time interval, only a single component was present  
808 in the two-dimensional NND distribution, located far in the upper right section of the space. This  
809 mode largely dissipated during the co-injection intervals and was replaced by clustered and

810 background components located closer to the center. As discussed in these studies, induced  
811 seismicity tends to increase earthquake rates locally and across limited time spans. This is  
812 reflected quite clearly in the joint NND distributions, where populations of the elevated induced  
813 background manifest more centrally and closer to the clustered population. This effect is starkly  
814 evident in regions governed by a low natural seismicity rate like the WCSB and Oklahoma,  
815 where the tectonic and induced background components can be separated by inspection, but is  
816 also discernable in naturally active areas such as California.

817 We also observed a tightly clustered earthquake subpopulation in the NND distributions,  
818 which occurred at very small inter-event distance values and appeared highly correlated with the  
819 loosely clustered background. We found that tightly clustered event sequences were nearly four  
820 times as likely to be strongly linked to a loosely clustered event compared to a natural  
821 background event. Both groups of earthquakes made up the entirety of discernable induced  
822 clustering in the region and both grew disparately in relative proportion over recent times,  
823 coinciding with the growing use of hydraulic fracturing technology. However, we discovered  
824 that different triggering mechanisms produced differences in the mixing proportions of these  
825 earthquake groups, with hydraulic fracturing operations resulting in much larger proportions of  
826 tightly clustered earthquakes than conventional hydrocarbon production and wastewater disposal.  
827 Based on the results in section 5, several further insights may be gathered regarding the induced  
828 seismic clustering within the WCSB. First, wherever fluid injection was suspected as the  
829 seismogenic mechanism, either through wastewater disposal or HF (i.e. the MC1, MC2 and  
830 FCC), the clustering appeared more swarm-like and reminiscent of ductile failure. The lone case  
831 of fluid extraction-related seismicity, the RMHC, resulted in an elevated background rate and  
832 occasional burst-like sequencing, more suggestive of brittle failure. Second, HF operations  
833 seemed to trigger greater swarm-like behavior than wastewater injection. Results of the NND  
834 and ETAS model applications indicated that the MC2 and FCC contained higher levels of swarm  
835 seismicity than did the MC1. This may have been a consequence of the differences in injection  
836 volume and rate between cases, as well as the horizontal orientation of many new HF wells,  
837 which allows fluid and stress perturbations to be forced through a much larger volume of rock in  
838 the short term (King, 2010; Smith & Montgomery, 2015). There is also a possibility that HF-  
839 induced swarms can occur predominantly at lower magnitude levels, as evidenced by the  
840 elevated Gutenberg-Richter  $b$ -value within the FCC. Third, HF is capable of, albeit less

841 frequently, triggering larger aftershock sequences, where the migrating fluid or stress  
842 perturbation may be traveling into the crystalline basement and interacting with critically  
843 stressed faults, similar to the triggering mechanism attributed to wastewater disposal. Fourth,  
844 these aftershock sequences appear to result in connected earthquakes that span longer time  
845 frames than do the swarms of comparable sequence size. The swarms within the MC2 and FCC  
846 are almost all tightly constrained in space and time relative to their size, which may correlate  
847 with the spatial and temporal extent of their associated stimulating HF operations. This also  
848 suggests that the two types of clusters are caused by different mechanisms; the bursts by fluid  
849 intermingling with critically oriented faults resulting in a large event, which *then* triggers  
850 multiple offspring events in a conventional aftershock manner, versus the swarms where no  
851 distinct mainshock is present, yet multiple offspring continue to transpire as the pumped fluid  
852 repeatedly disturbs nearby faults (Schultz, Stern, Novakovic, et al., 2015; Bao & Eaton, 2016;  
853 Eaton, 2018). A possible example of swarms being directly related to HF activity is the notable  
854 resemblance between the identified swarms in the FCC and the largest sequence in the MC2 near  
855 Dawson Creek, B.C. (Figure S12, clusters 1, 2, and 3, and Figure S11, cluster 1). They each  
856 occurred within kilometers of active HF operations and are structurally similar; the Dawson  
857 Creek swarm is a smaller-scale version of the FCC sequences (comparable events chained  
858 together with a rapid decay time, relative to its size). It is possible that the likenesses in the  
859 fundamental structuring of these clusters may be reflective of their shared triggering mechanism.  
860 The disparities in their size and scope may be due to factors such as different pumping  
861 rates/pressures/times or total volume of fluid injected, in addition to local geologic factors.

862 A critical issue with the models employed in this study are their dependence on  
863 earthquake sampling statistics, which vary in representative accuracy and precision based on  
864 sample size and variance. The associated uncertainties for the Gutenberg-Richter and ETAS  
865 parameter estimates can be quantified, although the ETAS parameter errors computed in this  
866 study were unstable and hence removed; this needs to be addressed in future work. The NND  
867 calculations are less well constrained. Zaliapin & Ben-Zion (2015) examined the potential  
868 artifacts of catalogue inconsistencies on the results of their cluster analyses within southern  
869 California. They found that location errors and short-term incompleteness can lead to an  
870 overestimation of background seismicity and a corresponding underestimation of clustered  
871 earthquakes. This phenomenon appears independent of any particular cluster identification

872 technique, as long as it is based upon parent-offspring relationships. With respect to the long-  
873 term regional completeness, Zaliapin & Ben-Zion (2013a) showed that NND distributions  
874 remain stable (up to a certain magnitude cut-off, after which the distribution becomes unimodal  
875 and contains only single events). In this study, we nevertheless introduce some bias by applying  
876 a cut-off below the regional estimated completeness level to enrich sampling. The networks  
877 contributing to the Composite Alberta Seismicity Catalogue have undergone numerous changes  
878 and improvements across time, particularly near areas of suspected induced activity including  
879 along the Duvernay and Montney formations (for details, we refer to Adams & Halchuk (2003)  
880 and Cui & Atkinson (2016)). This implies that the differences observed in earthquake  
881 distribution over time and between clusters may be partly the result of a changing  $M_c$ . However,  
882 we point to the disparate changes in rate between the earthquake subpopulations found in section  
883 4, which hold for cut-off magnitudes up to the regional estimated completeness (Figure S8), as  
884 well as the suspicious spatial relationship between the clustered events and human operations as  
885 evidence that the recent changes in earthquake distribution are significant, and not entirely due to  
886 the enhancement of the regional network.

## 887 **7 Conclusions**

888 A statistical analysis of catalogued seismicity within the Western Canada Sedimentary  
889 Basin (WCSB) was performed. We conducted a regional study in section 4, analyzing space-  
890 time-magnitude inter-event nearest-neighbour distance (NND) distributions across Alberta and  
891 eastern B.C. over time, beginning from the first observed instance of induced activity in 1975 up  
892 to the nearly present hydraulic fracturing (HF) related activity in 2018. Analysis over the entire  
893 time frame revealed the existence of a tri-modal inter-event distance distribution, where events  
894 generally appeared to occur either: (i) very closely together in space and time (within the tightly  
895 clustered mode); (ii) moderately close together (within the loosely clustered mode); or (iii) as a  
896 stationary, space-inhomogeneous Poisson process (the deep background). Analysis over  
897 separated time intervals demonstrated that a disproportionate increase in both the loosely and  
898 tightly clustered earthquake components occurred between 1975-2009 and 2010-2018, where the  
899 first interval predates the broad-scale implementation of HF technology. The first two modes of  
900 inter-event distance distribution are believed to reflect HF operation, wastewater disposal and  
901 conventional hydrocarbon production-related earthquakes. The third mode is inferred to

902 represent natural background seismicity, based on its uniform spatial distribution and large inter-  
903 event distances (resembling a point process). The spatial distribution of the natural background  
904 events contrasts with the localized loosely and tightly clustered subpopulations occurring at  
905 smaller inter-event distance values. We posit that the majority of induced activity occurs within  
906 these clustered modes, and that their increasing prevalence within the region is attributable to the  
907 growing usage of HF technology.

908 In section 5, we investigated four cases of induced seismic clustering within the WCSB.  
909 Frequency-magnitude statistics were assessed using the Gutenberg-Richter (GR) relation. Inter-  
910 event space-time-magnitude distributions and individual clustering properties were evaluated  
911 with the nearest-neighbour distance (NND) method and the epidemic type aftershock sequence  
912 (ETAS) model. It was determined that the seismicity triggered by conventional gas extraction  
913 near Rocky Mountain House (the RMHC) and the wastewater disposal-related earthquakes near  
914 Fort St. John (the MC1) primarily manifested as discrete events, loosely clustered in space and  
915 time, that occupied the middle mode of the inter-event NND distributions. These events were  
916 characterized by low-to-moderate GR  $b$ -values and poorer fits to the ETAS model. The few  
917 tightly clustered event sequences that did occur were small and decayed rapidly. The more recent  
918 clustering along the Montney formation (the MC2) also occupied the loosely clustered domain  
919 but contained an additional mode within the tightly clustered domain. These earthquakes were  
920 characterized by a slight increase in  $b$ -value from the previous period and were better fit by the  
921 ETAS model, with a reduced magnitude-sensitivity parameter. We identified more event  
922 sequences over this period, which were larger and more swarm-like. Finally, near Fox Creek (the  
923 FCC), substantial HF-related activity occurred almost entirely within the tightly clustered  
924 domain, in stark contrast with the previous clusters. These earthquakes formed a very steep  
925 frequency-magnitude distribution with a high  $b$ -value and fit the ETAS model exceptionally  
926 well, particularly when the background rate parameter was constrained to nearly zero, with a low  
927 magnitude sensitivity comparable to the MC2. The many detected event sequences were large,  
928 distinctly separable and overwhelmingly swarm-like.

## 929 **Acknowledgments and Data**

930 This work is supported by the Natural Sciences and Engineering Research Council of Canada  
931 and is a part of the Canadian Induced Seismicity Collaboration. The seismic database was

932 compiled from the Composite Alberta Seismicity Catalogue, available online at  
933 [www.inducedseismicity.ca](http://www.inducedseismicity.ca) (last accessed June 2020).

## 934 **References**

- 935 Adams, J., & Halchuk, S. (2003). Fourth Generation Seismic Hazard Maps of Canada: Values  
936 for Over 650 Canadian Localities Intended for the 2005 National Building Code of  
937 Canada. <https://doi.org/10.4095/214223>
- 938 Ader, T. J., & Avouac, J.-P. (2013). Detecting periodicities and declustering in earthquake  
939 catalogs using the Schuster spectrum, application to Himalayan seismicity. *Earth and*  
940 *Planetary Science Letters*, 377–378(Journal Article), 97–105.  
941 <https://doi.org/10.1016/j.epsl.2013.06.032>
- 942 Akaike, H. (1974). A new look at the statistical model identification. *IEEE Transactions on*  
943 *Automatic Control*, 19(6), 716–723. <https://doi.org/10.1109/TAC.1974.1100705>
- 944 Aki, K. (1965). Maximum Likelihood Estimate of  $b$  in the Formula  $\log N = a - bM$  and its  
945 Confidence Limits. *Bull. Earthq. Res. Inst. Tokyo Univ*, 43, 237–239.
- 946 Atkinson, G. M. (2017). Strategies to prevent damage to critical infrastructure due to induced  
947 seismicity. *FACETS*, 2(1), 374–394. <https://doi.org/10.1139/facets-2017-0013>
- 948 Atkinson, G. M., Eaton, D. W., Ghofrani, H., Walker, D., Cheadle, B., Schultz, R., et al. (2016).  
949 Hydraulic Fracturing and Seismicity in the Western Canada Sedimentary Basin.  
950 *Seismological Research Letters*, 87(3), 631–647. <https://doi.org/10.1785/0220150263>
- 951 Atkinson, G. M., Eaton, D. W., & Igonin, N. (2020). Developments in understanding seismicity  
952 triggered by hydraulic fracturing. *Nature Reviews Earth & Environment*, 1(5), 264–277.  
953 <https://doi.org/10.1038/s43017-020-0049-7>
- 954 Baiesi, M., & Paczuski, M. (2004). Scale-free networks of earthquakes and aftershocks. *Physical*  
955 *Review. E, Statistical, Nonlinear, and Soft Matter Physics*, 69(6).  
956 <https://doi.org/10.1103/PhysRevE.69.066106>
- 957 Bao, X., & Eaton, D. W. (2016). Fault activation by hydraulic fracturing in western Canada.  
958 *Science (New York, N.Y.)*, 354(6318), 1406–1409.  
959 <https://doi.org/10.1126/science.aag2583>

- 960 Baranova, V., Mustaqeem, A., & Bell, S. (1999). A model for induced seismicity caused by  
961 hydrocarbon production in the Western Canada Sedimentary Basin. *Canadian Journal of*  
962 *Earth Sciences*, 36(1), 47–64. <https://doi.org/10.1139/cjes-36-1-47>
- 963 B.C. Oil and Gas Commission. (2012). Investigation of observed seismicity in the Horn River  
964 Basin. Victoria, B.C.: BC Oil and Gas Commission.
- 965 B.C. Oil and Gas Commission. (2014). Investigation of observed seismicity in the Montney  
966 Trend. Victoria, B.C.: BC Oil and Gas Commission.
- 967 Ben-Zion, Y., & Lyakhovsky, V. (2006). Analysis of aftershocks in a lithospheric model with  
968 seismogenic zone governed by damage rheology. *Geophysical Journal International*,  
969 165(1), 197–210. <https://doi.org/10.1111/j.1365-246X.2006.02878.x>
- 970 Brodsky, E. E., & Lajoie, L. J. (2013). Anthropogenic Seismicity Rates and Operational  
971 Parameters at the Salton Sea Geothermal Field. *Science*, 341(6145), 543–546.  
972 <https://doi.org/10.1126/science.1239213>
- 973 Brudzinski, M. R., & Kozłowska, M. (2019). Seismicity induced by hydraulic fracturing and  
974 wastewater disposal in the Appalachian Basin, USA: a review. *Acta Geophysica*, 67(1),  
975 351–364. <https://doi.org/10.1007/s11600-019-00249-7>
- 976 Cao, A., & Gao, S. S. (2002). Temporal variation of seismic b-values beneath northeastern Japan  
977 island arc. *Geophysical Research Letters*, 29(9). <https://doi.org/10.1029/2001GL013775>
- 978 Clerc, F., Harrington, R. M., Liu, Y., & Gu, Y. J. (2016). Stress drop estimates and hypocenter  
979 relocations of induced seismicity near Crooked Lake, Alberta. *Geophysical Research*  
980 *Letters*, 43(13), 6942–6951. <https://doi.org/10.1002/2016GL069800>
- 981 Console, R., Jackson, D. D., & Kagan, Y. Y. (2010). Using the ETAS Model for Catalog  
982 Declustering and Seismic Background Assessment. *Pure and Applied Geophysics*,  
983 167(6), 819–830. <https://doi.org/10.1007/s00024-010-0065-5>
- 984 Cui, L., & Atkinson, G. M. (2016). Spatiotemporal Variations in the Completeness Magnitude of  
985 the Composite Alberta Seismicity Catalog (CASC). *Seismological Research Letters*,  
986 87(4), 853–863. <https://doi.org/10.1785/0220150268>

- 987 Cui, L., Fereidoni, A., & Atkinson, G. (2015). Compilation of Composite Alberta Seismicity  
988 Catalog (CASC) for Earthquake Hazard from Induced Seismicity in Alberta.
- 989 Deng, K., Liu, Y., & Harrington, R. M. (2016). Poroelastic stress triggering of the December  
990 2013 Crooked Lake, Alberta, induced seismicity sequence. *Geophysical Research*  
991 *Letters*, 43(16), 8482–8491. <https://doi.org/10.1002/2016GL070421>
- 992 Doglioni, C. (2018). A classification of induced seismicity. *Geoscience Frontiers*, 9(6), 1903–  
993 1909. <https://doi.org/10.1016/j.gsf.2017.11.015>
- 994 Eaton, D. W. (2018). *Passive seismic monitoring of induced seismicity: fundamental principles*  
995 *and application to energy technologies*. Cambridge University Press.
- 996 Eaton, D. W., & Mahani, A. B. (2015). Focal Mechanisms of Some Inferred Induced  
997 Earthquakes in Alberta, Canada. *Seismological Research Letters*, 86(4), 1078–1085.  
998 <https://doi.org/10.1785/0220150066>
- 999 Eaton, D. W., Igonin, N., Poulin, A., Weir, R., Zhang, H., Pellegrino, S., & Rodriguez, G.  
1000 (2018). Induced Seismicity Characterization during Hydraulic-Fracture Monitoring with  
1001 a Shallow-Wellbore Geophone Array and Broadband Sensors. *Seismological Research*  
1002 *Letters*, 89(5), 1641–1651. <https://doi.org/10.1785/0220180055>
- 1003 Farrell, J., Husen, S., & Smith, R. B. (2009). Earthquake swarm and b-value characterization of  
1004 the Yellowstone volcano-tectonic system. *Journal of Volcanology and Geothermal*  
1005 *Research*, 188(1), 260–276. <https://doi.org/10.1016/j.jvolgeores.2009.08.008>
- 1006 Gardner, J. K., & Knopoff, L. (1974). Is the sequence of earthquakes in Southern California,  
1007 with aftershocks removed, Poissonian? *Bulletin of the Seismological Society of America*,  
1008 64(5), 1363–1367.
- 1009 Ghofrani, H., & Atkinson, G. M. (2016). A preliminary statistical model for hydraulic fracture-  
1010 induced seismicity in the Western Canada Sedimentary Basin. *Geophysical Research*  
1011 *Letters*, 43(19), 172. <https://doi.org/10.1002/2016GL070042>
- 1012 Goebel, T. H. W., Hauksson, E., Aminzadeh, F., & Ampuero, J.-P. (2015). An objective method  
1013 for the assessment of fluid injection-induced seismicity and application to tectonically  
1014 active regions in central California. *Journal of Geophysical Research: Solid Earth*,  
1015 120(10), 7013–7032. <https://doi.org/10.1002/2015JB011895>

- 1016 Grigoli, F., Cesca, S., Priolo, E., Rinaldi, A. P., Clinton, J. F., Stabile, T. A., et al. (2017).  
1017 Current challenges in monitoring, discrimination, and management of induced seismicity  
1018 related to underground industrial activities: A European perspective. *Reviews of*  
1019 *Geophysics*, 55(2), 310–340. <https://doi.org/10.1002/2016RG000542>
- 1020 Hastie, T., Tibshirani, R., & Friedman, J. H. (2009). The EM Algorithm. In *The elements of*  
1021 *statistical learning: data mining, inference, and prediction* (2nd ed., pp. 236–243). New  
1022 York: Springer.
- 1023 Hicks, A. L. (2011). Clustering in multidimensional spaces with applications to statistical  
1024 analysis of earthquake clustering. ProQuest Dissertations Publishing.
- 1025 Horner, R. B., Barclay, J. E., & MacRae, J. M. (1994). Earthquakes and Hydrocarbon Production  
1026 in the Fort St. John Area of Northeastern British Columbia. *Canadian Journal of*  
1027 *Exploration Geophysics*, 30(1), 38–50.
- 1028 Horton, S. (2012). Disposal of Hydrofracking Waste Fluid by Injection into Subsurface Aquifers  
1029 Triggers Earthquake Swarm in Central Arkansas with Potential for Damaging  
1030 Earthquake. *Seismological Research Letters*, 83(2), 250–260.  
1031 <https://doi.org/10.1785/gssrl.83.2.250>
- 1032 Kagan, Y. Y. (1991). Fractal dimension of brittle fracture. *Journal of Nonlinear Science*, 1(1), 1–  
1033 16. <https://doi.org/10.1007/BF01209146>
- 1034 Keranen, K. M., & Weingarten, M. (2018). Induced Seismicity. *Annual Review of Earth and*  
1035 *Planetary Sciences*, 46(1), 149–174. [https://doi.org/10.1146/annurev-earth-082517-](https://doi.org/10.1146/annurev-earth-082517-010054)  
1036 [010054](https://doi.org/10.1146/annurev-earth-082517-010054)
- 1037 Keranen, K. M., Weingarten, M., Abers, G. A., Bekins, B. A., & Ge, S. (2014). Sharp increase in  
1038 central Oklahoma seismicity since 2008 induced by massive wastewater injection.  
1039 *Science*, 345(6195), 448–451. <https://doi.org/10.1126/science.1255802>
- 1040 Kettlety, T., Verdon, J. P., Werner, M. J., Kendall, J. M., & Budge, J. (2019). Investigating the  
1041 role of elastostatic stress transfer during hydraulic fracturing-induced fault activation.  
1042 *Geophysical Journal International*, (Journal Article). <https://doi.org/10.1093/gji/ggz080>
- 1043 Kettlety, T., Verdon, J. P., Werner, M. J., & Kendall, J. M. (2020). Stress Transfer From  
1044 Opening Hydraulic Fractures Controls the Distribution of Induced Seismicity. *Journal of*

- 1045 Geophysical Research: Solid Earth, 125(1), e2019JB018794.  
1046 <https://doi.org/10.1029/2019JB018794>
- 1047 King, G. E. (2010). Thirty Years of Gas Shale Fracturing: What Have We Learned? In SPE-  
1048 133456-MS (p. 50). SPE: Society of Petroleum Engineers.  
1049 <https://doi.org/10.2118/133456-MS>
- 1050 Kosobokov, V., & Mazhkenov, S. A. (2013). On Similarity in the Spatial Distribution of  
1051 Seismicity. In *Computational Seismology and Geodynamics* (Vol. 22).  
1052 <https://doi.org/10.1029/CS001p0006>
- 1053 Kumazawa, T., & Ogata, Y. (2013). Quantitative description of induced seismic activity before  
1054 and after the 2011 Tohoku-Oki earthquake by nonstationary ETAS models. *Journal of*  
1055 *Geophysical Research: Solid Earth*, 118(12), 6165–6182.  
1056 <https://doi.org/10.1002/2013JB010259>
- 1057 Langenbruch, C., & Shapiro, S. A. (2010). Decay rate of fluid-induced seismicity after  
1058 termination of reservoir stimulations. *Geophysics*, 75(6), MA53–MA62.  
1059 <https://doi.org/10.1190/1.3506005>
- 1060 Langenbruch, C., Ellsworth, W. L., Woo, J.-U., & Wald, D. J. (2020). Value at Induced Risk:  
1061 Injection-Induced Seismic Risk From Low-Probability, High-Impact Events. *Geophysical*  
1062 *Research Letters*, 47(2), e2019GL085878. <https://doi.org/10.1029/2019GL085878>
- 1063 Lee, K.-K., Ellsworth, W. L., Giardini, D., Townend, J., Ge, S., Shimamoto, T., et al. (2019).  
1064 Managing injection-induced seismic risks. *Science*, 364(6442), 730.  
1065 <https://doi.org/10.1126/science.aax1878>
- 1066 Lei, X., Yu, G., Ma, S., Wen, X., & Wang, Q. (2008). Earthquakes induced by water injection at  
1067 ~3 km depth within the Rongchang gas field, Chongqing, China. *Journal of Geophysical*  
1068 *Research - Solid Earth*, 113(B10), B10310. <https://doi.org/10.1029/2008JB005604>
- 1069 Llenos, A. L., & Michael, A. J. (2013). Modeling Earthquake Rate Changes in Oklahoma and  
1070 Arkansas: Possible Signatures of Induced Seismicity. *Bulletin of the Seismological*  
1071 *Society of America*, 103(5), 2850–2861. <https://doi.org/10.1785/0120130017>

- 1072 Llenos, A. L., & Michael, A. J. (2016). Characterizing potentially induced earthquake rate  
1073 changes in the Brawley Seismic Zone, southern California. *Bulletin of the Seismological*  
1074 *Society of America*, 106(5), 2045–2062. <https://doi.org/10.1785/0120150053>
- 1075 Lombardi, A. M., Cocco, M., & Marzocchi, W. (2010). On the Increase of Background  
1076 Seismicity Rate during the 1997-1998 Umbria-Marche, Central Italy, Sequence:  
1077 Apparent Variation or Fluid-Driven Triggering? *Bulletin of the Seismological Society of*  
1078 *America*, 100(3), 1138–1152. <https://doi.org/10.1785/0120090077>
- 1079 Maghsoudi, S., Eaton, D. W., & Davidsen, J. (2016). Nontrivial clustering of microseismicity  
1080 induced by hydraulic fracturing. *Geophysical Research Letters*, 43(20), 10-10,679.  
1081 <https://doi.org/10.1002/2016GL070983>
- 1082 Maghsoudi, S., Baró, J., Kent, A., Eaton, D., & Davidsen, J. (2018). Interevent Triggering in  
1083 Microseismicity Induced by Hydraulic Fracturing. *Bulletin of the Seismological Society*  
1084 *of America*, 108(3A), 1133–1146. <https://doi.org/10.1785/0120170368>
- 1085 Martínez-Garzón, P., Zaliapin, I., Ben-Zion, Y., Kwiatak, G., & Bohnhoff, M. (2018).  
1086 Comparative Study of Earthquake Clustering in Relation to Hydraulic Activities at  
1087 Geothermal Fields in California. *Journal of Geophysical Research: Solid Earth*, 123(5),  
1088 4041–4062. <https://doi.org/10.1029/2017JB014972>
- 1089 McClure, M., Gibson, R., Chiu, K.-K., & Ranganath, R. (2017). Identifying potentially induced  
1090 seismicity and assessing statistical significance in Oklahoma and California: Induced  
1091 Seismicity Statistics. *Journal of Geophysical Research: Solid Earth*, (Journal Article).  
1092 <https://doi.org/10.1002/2016JB013711>
- 1093 McGarr, A., & Barbour, A. J. (2017). Wastewater Disposal and the Earthquake Sequences  
1094 During 2016 Near Fairview, Pawnee, and Cushing, Oklahoma: Induced Earthquake  
1095 Sequences During 2016. *Geophysical Research Letters*, 44(18), 9330–9336.  
1096 <https://doi.org/10.1002/2017GL075258>
- 1097 Mogi, K. (1963). Some Discussions on Aftershocks, Foreshocks and Earthquake Swarms : the  
1098 Fracture of a Semi-infinite Body Caused by an Inner Stress Origin and Its Relation to the  
1099 Earthquake Phenomena (Third Paper). *Bull. Earthq. Res. Inst. Tokyo Univ*, 41, 615–658.

- 1100 Morita, Y., Nakao, S., & Hayashi, Y. (2006). A quantitative approach to the dike intrusion  
1101 process inferred from a joint analysis of geodetic and seismological data for the 1998  
1102 earthquake swarm off the east coast of Izu Peninsula, central Japan. *Journal of*  
1103 *Geophysical Research: Solid Earth*, 111(B6). <https://doi.org/10.1029/2005JB003860>
- 1104 Ogata, Y. (1988). Statistical Models for Earthquake Occurrences and Residual Analysis for Point  
1105 Processes. *Journal of the American Statistical Association*, 83(401), 9–27.  
1106 <https://doi.org/10.1080/01621459.1988.10478560>
- 1107 Ogata, Y. (1989). Statistical model for standard seismicity and detection of anomalies by residual  
1108 analysis. *Tectonophysics*, 169(1), 159–174. [https://doi.org/10.1016/0040-1951\(89\)90191-](https://doi.org/10.1016/0040-1951(89)90191-1)  
1109 1
- 1110 Ogata, Y. (1992). Detection of precursory relative quiescence before great earthquakes through a  
1111 statistical model. *Journal of Geophysical Research*, 97(B13), 19845.  
1112 <https://doi.org/10.1029/92JB00708>
- 1113 Omi, T., Ogata, Y., Hirata, Y., & Aihara, K. (2014). Estimating the ETAS model from an early  
1114 aftershock sequence. *Geophysical Research Letters*, 41(3), 850–857.  
1115 <https://doi.org/10.1002/2013GL058958>
- 1116 Omori, F. (1894). On the aftershocks of earthquakes. *Journal of the College of Science, Imperial*  
1117 *University of Tokyo*, (7), 111–200.
- 1118 Reasenberg, P. (1985). Second-order moment of central California seismicity, 1969–1982.  
1119 *Journal of Geophysical Research: Solid Earth*, 90(B7), 5479–5495.  
1120 <https://doi.org/10.1029/JB090iB07p05479>
- 1121 Rogers, G. C., & Horner, R. B. (1991). An Overview of Western Canadian Seismicity. In D. B.  
1122 Slemmons, E. R. Engdahl, M. D. Zoback, & D. D. Blackwell (Eds.), *Neotectonics of*  
1123 *North America* (Vol. 1, pp. 69–76). Geological Society of America.
- 1124 Sadovsky, M. A., Golubeva, T. V., Pisarenko, V. F., & Shninman, M. G. (1984). Characteristic  
1125 dimension of rocks and hierarchical properties of seismicity. *Izy. Acad. Sci. USSR. Phys.*  
1126 *Solid Earth*, 20, 87–95.

- 1127 Sagiya, T., Stein, R. S., & Toda, S. (2002). Evidence from the ad 2000 Izu islands earthquake  
1128 swarm that stressing rate governs seismicity. *Nature*, 419(6902), 58–61.  
1129 <https://doi.org/10.1038/nature00997>
- 1130 Schaefer, A. M., Daniell, J. E., & Wenzel, F. (2017). The smart cluster method: Adaptive  
1131 earthquake cluster identification and analysis in strong seismic regions. *Journal of*  
1132 *Seismology*, 21(4), 965–985. <https://doi.org/10.1007/s10950-017-9646-4>
- 1133 Schoenball, M., & Ellsworth, W. L. (2017). A Systematic Assessment of the Spatiotemporal  
1134 Evolution of Fault Activation Through Induced Seismicity in Oklahoma and Southern  
1135 Kansas. *Journal of Geophysical Research: Solid Earth*, 122(12), 10,189–10,206.  
1136 <https://doi.org/10.1002/2017JB014850>
- 1137 Schoenball, M., Davatzes, N. C., & Glen, J. M. G. (2015). Differentiating induced and natural  
1138 seismicity using space-time-magnitude statistics applied to the Coso Geothermal field.  
1139 *Geophysical Research Letters*, 42(15), 6221–6228.  
1140 <https://doi.org/10.1002/2015GL064772>
- 1141 Schultz, R., Stern, V., & Gu, Y. J. (2014). An investigation of seismicity clustered near the  
1142 Cordell Field, west central Alberta, and its relation to a nearby disposal well. *Journal of*  
1143 *Geophysical Research: Solid Earth*, 119(4), 3410–3423.  
1144 <https://doi.org/10.1002/2013JB010836>
- 1145 Schultz, R., Stern, V., Gu, Y. J., & Eaton, D. (2015). Detection Threshold and Location  
1146 Resolution of the Alberta Geological Survey Earthquake Catalogue. *Seismological*  
1147 *Research Letters*, 86(2A), 385–397. <https://doi.org/10.1785/0220140203>
- 1148 Schultz, R., Stern, V., Novakovic, M., Atkinson, G., & Gu, Y. J. (2015). Hydraulic fracturing  
1149 and the Crooked Lake Sequences: Insights gleaned from regional seismic networks.  
1150 *Geophysical Research Letters*, 42(8), 2750–2758. <https://doi.org/10.1002/2015GL063455>
- 1151 Schultz, R., Mei, S., Pană, D., Stern, V., Gu, Y. J., Kim, A., & Eaton, D. (2015). The Cardston  
1152 Earthquake Swarm and Hydraulic Fracturing of the Exshaw Formation (Alberta Bakken  
1153 Play). *Bulletin of the Seismological Society of America*, 105(6), 2871–2884.  
1154 <https://doi.org/10.1785/0120150131>

- 1155 Schultz, R., Corlett, H., Haug, K., Kocon, K., MacCormack, K., Stern, V., & Shipman, T.  
1156 (2016). Linking fossil reefs with earthquakes: Geologic insight to where induced  
1157 seismicity occurs in Alberta. *Geophysical Research Letters*, 43(6), 2534–2542.  
1158 <https://doi.org/10.1002/2015GL067514>
- 1159 Schultz, R., Wang, R., Gu, Y. J., Haug, K., & Atkinson, G. (2017). A seismological overview of  
1160 the induced earthquakes in the Duvernay play near Fox Creek, Alberta. *Journal of*  
1161 *Geophysical Research: Solid Earth*, 122(1), 492–505.  
1162 <https://doi.org/10.1002/2016JB013570>
- 1163 Schultz, R., Atkinson, G., Eaton, D. W., Gu, Y. J., & Kao, H. (2018). Hydraulic fracturing  
1164 volume is associated with induced earthquake productivity in the Duvernay play.  
1165 *Science*, 359(6373), 304–308. <https://doi.org/10.1126/science.aao0159>
- 1166 Schultz, R., Skoumal, R. J., Brudzinski, M. R., Eaton, D., Baptie, B., & Ellsworth, W. (2020).  
1167 Hydraulic Fracturing Induced Seismicity. *Reviews of Geophysics*, e2019RG000695.  
1168 <https://doi.org/10.1029/2019RG000695>
- 1169 Schwarz, G. (1978). Estimating the Dimension of a Model. *Ann. Statist.*, 6(2), 461–464.  
1170 <https://doi.org/10.1214/aos/1176344136>
- 1171 Scuderi, M. M., Collettini, C., & Marone, C. (2017). Frictional stability and earthquake  
1172 triggering during fluid pressure stimulation of an experimental fault. *Earth and Planetary*  
1173 *Science Letters*, 477(Journal Article), 84–96. <https://doi.org/10.1016/j.epsl.2017.08.009>
- 1174 Segall, P. (1985). Stress and subsidence resulting from subsurface fluid withdrawal in the  
1175 epicentral region of the 1983 Coalinga Earthquake. *Journal of Geophysical Research*,  
1176 90(B8), 6801. <https://doi.org/10.1029/JB090iB08p06801>
- 1177 Segall, P., Grasso, J., & Mossop, A. (1995). Poroelastic stressing and induced seismicity near the  
1178 Lacq gas field, southwestern France. *International Journal of Rock Mechanics and*  
1179 *Mining Sciences and Geomechanics Abstracts*, 32(4), A152–A152.  
1180 [https://doi.org/10.1016/0148-9062\(95\)96941-4](https://doi.org/10.1016/0148-9062(95)96941-4)
- 1181 Shi, Y., & Bolt, B. (1982). The standard error of the magnitude-frequency b value. *Bulletin of*  
1182 *the Seismological Society of America*, 72(5), 1677.

- 1183 Skoumal, R. J., Brudzinski, M. R., & Currie, B. S. (2015). Earthquakes Induced by Hydraulic  
1184 Fracturing in Poland Township, Ohio. *Bulletin of the Seismological Society of America*,  
1185 105(1), 189–197. <https://doi.org/10.1785/0120140168>
- 1186 Smith, M. B., & Montgomery, C. T. (2015). *Hydraulic fracturing*. Boca Raton, Florida: CRC  
1187 Press.
- 1188 Utsu, T. (1961). A statistical study of the occurrence of aftershocks. *Geophysical Magazine*,  
1189 (30), 521–605.
- 1190 Utsu, T. (1966). A Statistical Significance Test of the Difference in b-value between Two  
1191 Earthquake Groups. *Journal of Physics of the Earth*, 14(2), 37–40.  
1192 <https://doi.org/10.4294/jpe1952.14.37>
- 1193 Utsu, T. (1970). Aftershocks and earthquake statistics (II) - Further investigation of aftershocks  
1194 and other earthquake sequences based on a new classification of earthquake sequences. *J.*  
1195 *Fac. Sci. Hokkaido Univ.*, 3, 197–266.
- 1196 Vasylykivska, V. S., & Huerta, N. J. (2017). Spatiotemporal distribution of Oklahoma  
1197 earthquakes: Exploring relationships using a nearest-neighbor approach. *Journal of*  
1198 *Geophysical Research: Solid Earth*, 122(7), 5395–5416.  
1199 <https://doi.org/10.1002/2016JB013918>
- 1200 Wang, R., Gu, Y. J., Schultz, R., Kim, A., & Atkinson, G. (2016). Source analysis of a potential  
1201 hydraulic-fracturing-induced earthquake near Fox Creek, Alberta. *Geophysical Research*  
1202 *Letters*, 43(2), 564. <https://doi.org/10.1002/2015GL066917>
- 1203 Wetmiller, R. J. (1986). Earthquakes near Rocky Mountain House, Alberta, and their relationship  
1204 to gas production facilities. *Canadian Journal of Earth Sciences*, 23(2), 172–181.  
1205 <https://doi.org/10.1139/e86-020>
- 1206 Wiemer, S., & Wyss, M. (2000). Minimum Magnitude of Completeness in Earthquake Catalogs:  
1207 Examples from Alaska, the Western United States, and Japan. *Bulletin of the*  
1208 *Seismological Society of America*, 90(4), 859–869. <https://doi.org/10.1785/0119990114>
- 1209 Zaliapin, I., & Ben-Zion, Y. (2013a). Earthquake clusters in southern California I: Identification  
1210 and stability. *Journal of Geophysical Research: Solid Earth*, 118(6), 2847–2864.  
1211 <https://doi.org/10.1002/jgrb.50179>

- 1212 Zaliapin, I., & Ben-Zion, Y. (2013b). Earthquake clusters in southern California II: Classification  
1213 and relation to physical properties of the crust. *Journal of Geophysical Research: Solid*  
1214 *Earth*, 118(6), 2865–2877. <https://doi.org/10.1002/jgrb.50178>
- 1215 Zaliapin, I., & Ben-Zion, Y. (2015). Artefacts of earthquake location errors and short-term  
1216 incompleteness on seismicity clusters in southern California. *Geophysical Journal*  
1217 *International*, 202(3), 1949–1968. <https://doi.org/10.1093/gji/ggv259>
- 1218 Zaliapin, I., & Ben-Zion, Y. (2016). Discriminating Characteristics of Tectonic and Human-  
1219 Induced Seismicity. *Bulletin of the Seismological Society of America*, 106(3), 846–859.  
1220 <https://doi.org/10.1785/0120150211>
- 1221 Zaliapin, I., Gabrielov, A., Keilis-Borok, V., & Wong, H. (2008). Clustering analysis of  
1222 seismicity and aftershock identification. *Physical Review Letters*, 101(1), 018501.  
1223 <https://doi.org/10.1103/PhysRevLett.101.018501>
- 1224 Zhang, H., Eaton, D. W., Rodriguez, G., & Jia, S. Q. (2019). Source-Mechanism Analysis and  
1225 Stress Inversion for Hydraulic-Fracturing-Induced Event Sequences near Fox Creek,  
1226 Alberta. *Bulletin of the Seismological Society of America*, 109(2), 636–651.  
1227 <https://doi.org/10.1785/0120180275>
- 1228 Zhuang, J., Ogata, Y., & Vere-Jones, D. (2004). Analyzing earthquake clustering features by  
1229 using stochastic reconstruction. *Journal of Geophysical Research - Solid Earth*, 109(B5),  
1230 B05301-n/a. <https://doi.org/10.1029/2003JB002879>
- 1231